Application of the lattice-Boltzmann method for simulating attachment of ink particles in paper

Timo Riikilä

MSc Thesis
University of Jyväskylä, Department of Physics
22nd November 2012
Supervisors: Keijo Mattila
Jussi Timonen

Tiivistelmä

Tässä Pro gradu -tutkielmassa esitellään hila-Boltzmann-menetelmän perusominaisuudet. Tämän lisäksi hila-Boltzmann menetelmän kanssa yhdessä käytetty partikkelimalli esitellään ja yhdistettyä mallia käytetään musteen etenemisen tutkimiseen paperinäytteissä. Simulointigeometrioiden hankkimiseen käytettiin kahta eri menetelmää, konfokaalimikroskopiaa ja röntgentomografiaa. Simulaatioparametrien ja paperin ominaisuuksien vaikutusta musteen etenemiseen tutkittiin. Kummallakin kuvanhankintamenetelmällä saatiin lupaavia tuloksia, mutta jotta simuloinnit ja kokeelliset tulokset saataisiin yhteneväisemmiksi, tulisi nämä kuvausmenetelmät yhdistää. Näin pystyttäisiin saamaan kuvia, joissa näkyy koko paperinäytteen paksuus yhdessä mustejakauman kanssa. Konfokaalimikroskooppikuvista saatuihin geometrioihin tehdyissä simulaatioissa varioitiin simulaatioparametrejä ja huomattiin että diffuusiokerroin oli ainut parametri, joka aiheutti huomattavan muutoksen mustejakaumissa. Tämä tukee intuitiivisesti odotettavaa tulosta; muste pyrkii liikkumaan suurien virtauskanavien suuntaisesti, ellei diffuusio ole riittävän voimakas erottaakseen huomattavan osan mustepartikkeleista virtauksesta. Eri määrän pohja- ja pintaliimaa sisältäviä näytteitä tutkittiin ja tulokset olivat osittain epäjohdonmukaisia. Toisessa simulointisarjassa mittaustulokset olivat yhteneviä kokeellisten tulosten kanssa kun taas toisessa eivät. Mahdollisia selityksiä tähän ovat muun muassa paperin heterogeenisyyden vaikutus tuloksiin, erot paperin ominaisuuksissa makroskooppisesti eri kohdissa paperia ja kemialliset ilmiöt joita ei otettu huomioon mallissa. Voimme kuitenkin päätellä, että simulaatiomenetelmät joita käytettiin kuvaavat pääpiirteittäin musteen tarttumista paperiin. Tämä päätelmä perustuu osaltaan siihen, että kokeellisesti havaittu jakaantuminen kahteen erilliseen komponenttiin mustepigmenttien jakaumassa näkyi myös simulaatiotuloksissa.

Abstract

In this thesis the basic properties of the lattice- Boltzmann method (LBM) are introduced. Also, a particle model used in combination with LBM is presented, and the combined model is then applied to ink propagation in samples of paper. Simulation geometries were acquired with two different methods, namely confocal microscopy and X-ray tomography. The effect of simulation parameters and paper properties on ink propagation was considered. Promising results were acquired with both image acquiring techniques, but for a better consistency between simulations and experiments the methods should be combined so as to get images that include the full thickness of the sample together with the ink distribution. Adjustment of simulation parameters in confocal microscopy geometries showed that diffusion coefficient was the main parameter that explained the form of the ink distribution curves. This suggests an intuitively expected result: ink tends to move with the major flow channels unless diffusion is strong enough to separate enough of ink particles from the flow. Simulations done in samples of varying sizing gave incoherent results. One simulation series was in agreement with experimental results, while another was not. Possible explanations to this dilemma includes effects of paper heterogeneity on the results, differencies in paper properties in macroscopically different parts of the paper, and chemical effects not taken into consideration in the model. We can conclude however that simulations with the methods applied here qualitatively capture the main features of the settling in paper. In part this conclusion is based in the fact that the experimentally observed division into two separate components in the distribution of attached ink pigments was also realised in the simulations.

Acknowledgements

Jill Tarter once said "The story of humans is the story of ideas. Scientific ideas that shine light into dark corners". When I started this thesis project roughly one year ago, I felt like there was no light in the corners nor in the entire room where I was standing. The method to be used was not familiar to me at all. What made the room even darker was the fact that my supervisor Keijo was about to move to the other side of the world. What came however clear in the following months was that the room got all the time brighter and brighter. Every e-mail I got from Keijo was like a glimpse of light, which deepened my understanding of the subject. So I would like to express my deepest gratitude to my supervisor Dr. Keijo Mattila for your advice and guidance.

I would also like to thank Professor Jussi Timonen and Dr. Markko Myllys for offering me this thesis project. Thanks also to Jussi for your encouragement, contructive suggestions and patience in improving my writing. I am also grateful to Dr. Jari Hyväluoma for your insightful ideas and advice on how to modify the model for the needs of this thesis, Roope Lehto for providing confocal microscopy images and help in analysis of the results and Axel Ekman for providing X-ray tomography images. Thanks also to the University of Jyväskylä for funding my research, this is thankfully acknowledged. Furthermore, I heartily thank all the members of room FL125 for the great conversations and laughs we have had together. The working days have passed rapidly in your delightful company. Last but not least, I am deeply grateful to my family and friends, especially to my fiancé Virva, for your endless support during this thesis project and all the years of studying. It seems to me that even the corners are starting to brighten.

Contents

1 Introduction **5**

2 Different approaches to fluid mechanics **7**

2.1 The macroscopic approach 7

2.2 From microscopic to mesoscopic 11

2.3 The Boltzmann equation 13

3 The lattice-Boltzmann method **18**

3.1 Derivation of the lattice-Boltzmann equation 18

3.2 Lattice-Boltzmann models 22

3.3 Boundary conditions and simulation geometries 27

4 Simulating fluid-particle suspensions **32**

4.1 Mathematical model for particle dynamics 32

4.2 Velocity Verlet algorithm 33

4.3 Wall attachment and particle restrictions 34

5 Simulations **36**

5.1 Simulations in confocal microscopy images 38

5.2 Simulations in X-ray tomography images 45

6 Conclusions **49**

1 Introduction

The exponential increase in the computing capacity has opened new doors to scientists in the last few decades. This has had an impact in particular on computational fluid dynamics. Computational methods have grown to be an equal contributer to the scientific development amongst the more traditional methods, namely experiments and theory.

The benefits of using computational methods in addition to the traditional ones are significant. First of all analytical solutions to fluid dynamics equations are sometimes hard or even impossible to find, and their numerical treatment is thus necessary. Experiments could also be done to gain knowledge in such a situation, but many times computational methods are more effective as there is no need to build expensive measurement set-ups, and adjustments in the conditions are far easier to do in a simulation set-up than in a physical system. Secondly, computational methods have some benefits over the experimental ones when it comes to analysis of the results. It is not possible to build an experimental set-up, where the relevant fluid-dynamical variables can be determined everywhere in the measurement domain, and measurement instruments often disturb the flow they monitor. Computational methods easily provide such information without disturbing the flow.

Traditionally methods in computational fluid dynamics simulate the Navier-Stokes equation, and a vast majority of commercial and non-commercial software are based on solving this equation. However new methods are arising that challenge the more traditional ones. One of them is the lattice-Boltzmann method in which a statistical approach on fluid-dynamical problems is taken. The method is very versatile and it can be used to simulate a number of different behaviours, including unsteady flows, phase separation, evaporation, condensation, cavitation, boyancy, flow in porous media and liquid-particle suspensions.

This thesis introduces the basic concepts of the lattice-Boltzmann method combined with a particle model used to simulate fluid-particle suspensions. Whole

books are written about the lattice-Boltzmann method so we stress here that the introduction is very compact and contains only main parts without any subtleties. More information on the subject can be found e.g. in Refs [1] and [2].

The model presented is used in the simulation part of this thesis to study the behaviour of ink particles propagating in paper. It is very beneficial to get a better understanding of the processes of ink propagation because it possibly has a strong effect on print quality. Thus far these processes are not fully understood, and the lattice-Boltzmann method can provide information that can not be extracted from experimental or analytical results.

2 Different approaches to fluid mechanics

Fluid mechanical problems can be approached at different levels of abstraction. At the most fundamental level, that of particles, the fluid is described by motion of individual particles and their mutual interactions. This kind of approach describes the flow in a very detailed manner. At the continuum level such details are omitted and the continuum assumption is made. The fluid is described no longer by motion of individual particles but rather with macroscopic state variables, such as pressure and density, which describe the fluid as a continuous material. Between the two aforementioned levels is an intermediate level in which a compromise between the two is pursued. The particle, continuum and intermediate levels correspond to microscopic, macroscopic and mesoscopic physical scales, respectively. The different levels of abstraction are illustrated in Fig. 1.

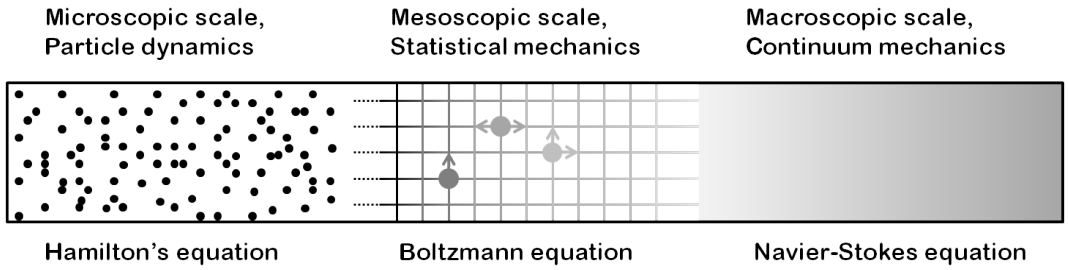

Figure 1: Different levels of abstraction of a physical system. Examples of governing equations are also shown.

Different approaches use different premises and by using these premises they arrive at different mathematical descriptions of the system, which have their strengths and weaknesses. Some standard mathematical models are reviewed in the following sections.

2.1 The macroscopic approach

Let us start our analysis of different mathematical descriptions of fluid from the viewpoint of continuum mechanics, where the dynamics of the system is

typically described with balance or conservation equations for the relevant hydrodynamic variables. For example, the general form of the conservation of mass can be expressed in the form

$$\frac{\partial \rho}{\partial t} + \nabla \cdot (\rho \mathbf{u}) = 0, \tag{1}$$

where ρ and $\mathbf{u} = (u, v, w)$ are the local density and velocity of the fluid, respectively. In what follows, we derive an equation for the conservation of momentum; Eq. (1) can be derived in a similar manner. By applying the Reynolds transport theorem to the linear momentum $\mathbf{p}_s$, an equation can be found for the rate of change of the momentum of a infinitesimal volume element [3],

$$\frac{d\mathbf{p}_s}{dt} = \sum \mathbf{F} = \frac{d}{dt}\left(\int_V \rho \mathbf{u}\, dV\right) + \int_S \mathbf{u}\rho(\mathbf{u}\cdot\mathbf{n})\, dA. \tag{2}$$

Here $\sum \mathbf{F}$ is the total force applied to the volume element. The first integral on the right hand side of the equation is over the volume element and the second over the area enclosing this volume; $\mathbf{n}$ is an outward unit normal vector of the surface. The second integral can be modified to one over the volume using the Gauss' theorem [4]:

$$\int_S \mathbf{u}\rho(\mathbf{u}\cdot\mathbf{n})\, dA = \int_V \left[\mathbf{u}\nabla\cdot\rho\mathbf{u} + (\rho\mathbf{u}\cdot\nabla)\mathbf{u}\right] dV. \tag{3}$$

The first term on the right hand side of Eq. (2) can also be modified using the Leibniz rule [5]:

$$\frac{d}{dt}\left(\int_V \rho \mathbf{u}\, dV\right) = \int_V \left[\rho\frac{\partial \mathbf{u}}{\partial t} + \mathbf{u}\frac{\partial \rho}{\partial t}\right] dV. \tag{4}$$

Substitution of Eqs (3) and (4) into Eq. (2) gives

$$\sum \mathbf{F} = \int_V \left[\rho\frac{\partial \mathbf{u}}{\partial t} + \mathbf{u}\frac{\partial \rho}{\partial t} + \mathbf{u}\nabla\cdot\rho\mathbf{u} + (\rho\mathbf{u}\cdot\nabla)\mathbf{u}\right] dV. \tag{5}$$

Rearranging the terms in Eq. (5), we can express it in the form

$$\sum \mathbf{F} = \int_V \left[\mathbf{u} \left(\frac{\partial \rho}{\partial t} + \nabla \cdot \rho \mathbf{u} \right) + \rho \left(\frac{\partial \mathbf{u}}{\partial t} + \mathbf{u} \cdot \nabla \mathbf{u} \right) \right] \, dV. \tag{6}$$

The total force applied to the volume element can be divided into body forces and surface forces:

$$\sum \mathbf{F} = \mathbf{F}_b + \mathbf{F}_s. \tag{7}$$

The body forces are due to external fields and act evenly on the entire mass within the volume. The only body force that is now taken into account is gravity, and its contribution takes the form

$$\mathbf{F}_{body} = \int_V \rho \mathbf{g} \, dV, \tag{8}$$

where $\mathbf{g}$ is the acceleration of gravity. The force caused by the internal stresses of the fluid to the surface element dA is

$$d\mathbf{F}_{surface} = \vec{\boldsymbol{\sigma}} \cdot \mathbf{n} \, dA, \tag{9}$$

where $\vec{\boldsymbol{\sigma}}$ is an appropriate stress tensor for the fluid. The total force applied to the surface of volume V is hence

$$\mathbf{F}_{surface} = \int_S \vec{\boldsymbol{\sigma}} \cdot \mathbf{n} \, dA = \int_V \nabla \cdot \vec{\boldsymbol{\sigma}} \, dV. \tag{10}$$

Above we have again applied the Gauss' theorem in transforming a surface integral into a volume integral. By combining Eqs (6)-(10), we get a volume integral equation for the conservation of linear momentum

$$\int_V \rho \mathbf{g} \, dV + \int_V \nabla \cdot \vec{\boldsymbol{\sigma}} \, dV = \int_V \left[\mathbf{u} \left(\frac{\partial \rho}{\partial t} + \nabla \cdot \rho \mathbf{u} \right) + \rho \left(\frac{\partial \mathbf{u}}{\partial t} + \mathbf{u} \cdot \nabla \mathbf{u} \right) \right] \, dV.$$

$$\Leftrightarrow \int_V \left[\rho\mathbf{g} + \nabla\cdot\vec{\boldsymbol{\sigma}} - \mathbf{u}\left(\frac{\partial\rho}{\partial t} + \nabla\cdot\rho\mathbf{u}\right) - \rho\left(\frac{\partial\mathbf{u}}{\partial t} + \mathbf{u}\cdot\nabla\mathbf{u}\right)\right]\, dV = 0. \tag{11}$$

The third term on the left hand side of the equation vanishes due to the equation of continuity Eq. (1), and the last term is the total acceleration of the fluid, i.e. $d\mathbf{u}/dt$ [3]. Since the integral is over an arbitrary volume element, the integrand itself must be zero and we arrive at

$$\rho\mathbf{g} + \nabla\cdot\vec{\boldsymbol{\sigma}} = \rho\frac{d\mathbf{u}}{dt}. \tag{12}$$

The stress tensor can be divided into viscous stresses $\vec{\boldsymbol{\tau}}$ and hydrostatic pressure $-p\vec{\boldsymbol{I}}$ acting on the surfaces of the volume element, giving us the final form of the conservation equation for the linear momentum:

$$\rho\mathbf{g} - \nabla p + \nabla\cdot\vec{\boldsymbol{\tau}} = \rho\frac{d\mathbf{u}}{dt}. \tag{13}$$

In order to derive the standard Navier-Stokes equations, three more assumptions have to be made. First of all, the fluid must be considered as incompressible, which is a fair assumption for many practical fluid flows. Secondly, one must assume that the fluid has a linear relation between applied shear stress and resulting strain rate, i.e. the fluid is assumed to be Newtonian. The third assumption required is isotropy of the fluid, which means that the properties of the fluid do not depend on the direction. Finally, by using these assumptions, one arrives at the expression

$$\rho\mathbf{g} - \nabla p + \mu\nabla^2\mathbf{u} = \rho\left[\frac{\partial\mathbf{u}}{\partial t} + \mathbf{u}\cdot\nabla\mathbf{u}\right]. \tag{14}$$

Eq. (14) is the Navier-Stokes equation which is a second-order nonlinear partial differential equation. Only a small number of analytical solutions for it are known. However numerical solutions can be obtained for a wide variety of

complex two- and three-dimensional flows.

The key assumption made when deriving the Navier-Stokes equation was the continuity of the fluid. Knudsen number is the ratio of the mean free path l_m of fluid particles to a charasteristic length scale L of the macroscopic system. That is, a low Knudsen number implies that the continuum assumption is valid. On the other hand, when dealing with very small length scales or under certain conditions, e.g. rarefied gas flows (high Knudsen number), the continuum assumption is invalid and hence the Navier-Stokes description compromised. One thus has to look for an alternative approach which does not suffer from the same limitations. One possibility is to construct a more general hydrodynamic equation such as e.g. the Burnett equation so as to cover a wider range of fluid flow situations [6, 7]. Alternatively, one can use an approach which does not assume that the fluid is continuous. Obviously with this latter choice we are moving towards a more detailed, microscopic description.

2.2 From microscopic to mesoscopic

In a small enough scale the fluid cannot be treated as a continuum and a more detailed description is necessary. Let us start our treatment of the topic by presenting the equation of motion and initial conditions for each molecule in an N molecule system. They can be expressed in the form

$$m_i \frac{d^2\mathbf{x}_i}{dt^2} = \mathbf{F}_i, \qquad \mathbf{u}_i(t=0) = \mathbf{u}_{i0}, \qquad \mathbf{x}_i(t=0) = \mathbf{x}_{i0}, \tag{15}$$

where m_i is the mass of molecule i, $\mathbf{u}_i = d\mathbf{x}_i/dt$ is its velocity and $\mathbf{F}_i$ is the force acting on molecule i due to intermolecular interactions. Any macroscopic system under normal conditions contains a number of molecules of the order of Avogadro's number ($\sim 6 \times 10^{23}$). A daunting computational challenge, to say the least. Even if this amount of data could be stored for a computer simulation, the problem of instability would remain. Even a tiny uncertainty in the initial conditions of the system could blow up exponentially in time, thereby destroing the predictive capability of the model.

In summary, molecular dynamics can provide a very detailed description, but is limited to rather small systems. An alternative description, a compromise between details and system size, can be derived using statistical mechanics. Instead of presenting the state of N molecules by equations (15), a phase space is defined with $6N$ mutually orthogonal axes, and each of them is associated with a position or momentum component of a molecule. Next a large number M of distinct systems is defined, which macroscopically are equivalent to the actual system considered. The microscopic states of the replicates can however differ greatly. This collection of replicates is referred to as the *Gibbs ensemble* [8]. Each replicate is presented by a point in the phase space $\mathbf{q}^k$, $k = 1, \ldots, M$. If a large enough value for the number of these replicates is assumed, one can describe their distribution in the phase space by a continuous density function. A normalisation can be done so that this density becomes a probability density denoted by $F_N = F_N(\mathbf{r}_1, \mathbf{p}_1, \ldots, \mathbf{r}_N, \mathbf{p}_N, t) = F_N(\mathbf{q}_1, \ldots, \mathbf{q}_N, t)$ with $\mathbf{q}_i = \mathbf{p}_i \mathbf{r}_i$. The evolution equation for this propability density is derived for example in Ref. [9], but here only the result is shown:

$$\frac{\partial F_N}{\partial t} + \sum_{i=1}^{N} \mathbf{c}_i \cdot \frac{\partial F_N}{\partial \mathbf{r}_i} + \sum_{i=1}^{N} \mathbf{F}_i \cdot \frac{\partial F_N}{\partial \mathbf{p}_i} = 0, \tag{16}$$

where $\mathbf{F}_i$ is the force acting on the molecule i. Equation (16) describes the conservation of the propability density and is called the Liouville's theorem. Equation (16) is in no way easier to solve than the original microscopic description Eq. (15). The amount of degrees of freedom is the same. The merit of the new equation comes from the fact that Liouville's theorem is a stepping stone for a procedure where details of the description can be systematically reduced. The N particle distribution function can simply be integrated over unwanted coordinates to arrive at a so called R particle reduced distribution function

$$F_R(\mathbf{q}_1, ..., \mathbf{q}_R, t) = \int F_N(\mathbf{q}_1, ..., \mathbf{q}_N, t) d\mathbf{q}_{R+1} \cdots d\mathbf{q}_N. \tag{17}$$

So as to find equations for the time development of these distribution functions,

one starts from the Liouville's theorem Eq. (16) and integrates each term over the coordinates $\mathbf{q}_{R+1}, \ldots, \mathbf{q}_N$. If a two particle potential

$$\mathbf{F}_i = -\sum_{j=1\neq i}^{N} \frac{\partial \phi_{ij}}{\partial \mathbf{q}_i} \tag{18}$$

is used, it is possible to find the time development of the reduced R particle distribution function such that

$$\frac{\partial F_R}{\partial t} + \sum_{i=1}^{R} \frac{\mathbf{p}_i}{m} \cdot \frac{\partial F_R}{\partial \mathbf{q}_i} - \sum_{i,j=1}^{R} \frac{\partial \phi_{ij}}{\partial \mathbf{q}_i} \cdot \frac{\partial F_R}{\partial \mathbf{p}_i} = (N-R) \int d\mathbf{r}_{R+1} \sum_{i=1}^{R} \frac{\partial \phi_{iR+1}}{\partial \mathbf{q}_i} \cdot \frac{\partial F_{R+1}}{\partial \mathbf{p}_i}. \tag{19}$$

Equation (19) is called the BBGKY hierarchy of equations named after Bogoliubov, Born, Green, Kirkwood and Yvon, who independently derived this equation [10]. A more rigorous derivation of this equation is given in Refs [1] and [11]. By writing down the equation for the first reduced distribution function,

$$\frac{\partial F_1}{\partial t} + \frac{\mathbf{p}_1}{m} \cdot \frac{\partial F_1}{\partial \mathbf{q}_1} = (N-1) \int d\mathbf{r}_2 \phi'_{12} \cdot \frac{\partial F_2}{\partial \mathbf{p}_1}, \tag{20}$$

one can immediately see that a completely new problem arises. Equation (19) is not closed: every distribution function F_R depends on the distribution function F_{R+1}. Usually the first reduced distribution function is of greatest interest, and therefore the next goal is to remove the F_2 dependence so that Eq. (20) becomes self-contained in F_1.

2.3 The Boltzmann equation

It was Ludwig Eduard Boltzmann who first published a closed equation for F_1 in 1872 [12]. He did not derive his famous equation by using Liouville's theorem nor the BBGKY hierarchy as a starting point. Boltzmann used instead a more intuitive approach. The Boltzmann equation can be derived also rigorously from the Liouville's theorem and BBGKY hierarchy, as is done for example in

Refs [1] and [11]. Here merely the underlying assumptions and the result of the derivation are presented. The assumptions are [13]:

1. The gas is assumed dilute enough so that all effects involving more than two particles can be neglected.

2. Collisions are assumed to be localised in both space and time, i.e. the duration of a collision is very small compared to the typical time scale of the system.

3. Collisions are assumed to be elastic: total mass, momentum and kinetic energy are conserved.

4. Collisions are also assumed to be microreversible. In a purely deterministic way this means that microscopic dynamics are time reversible. In a probabilistic way this means that the probability that the velocities (u', v') are changed into (u, v) in a collision process is the same as the probability that (u, v) are changed into (u', v').

5. The last required assumption is that of Boltzmann chaos: the velocities of two particles which are about to collide are uncorrelated.

Using these assumptions Boltzmann was able to derive his by now famous equation

$$\frac{\partial f}{\partial t} + \mathbf{c} \cdot \frac{\partial f}{\partial \mathbf{r}} + \mathbf{a} \cdot \frac{\partial f}{\partial \mathbf{c}} = \frac{1}{m} \int B(V_R, \theta)(\overline{f}\ \overline{f}_R - f\ f_R)\ d\epsilon\, d\theta\, d\mathbf{c}_R. \tag{21}$$

Note that Eq. (21) does not give the time development of F_1, but instead the development of mass density $f(\mathbf{r}_1, \mathbf{c}_1, t) = m \cdot N \cdot F_1(\mathbf{r}_1, \mathbf{c}_1, t)$. Here $\mathbf{a}$ is the acceleration due to force $\mathbf{F} = m\mathbf{a}$ and standard abbreviations have been used: $\overline{f} = f(\mathbf{r}, \overline{\mathbf{c}}, t)$, $\overline{f}_R = f(\mathbf{r}, \overline{\mathbf{c}}_R, t)$ and $f_R = f(\mathbf{r}, \mathbf{c}_R, t)$; $\overline{\mathbf{c}}$ and $\overline{\mathbf{c}}_R$ are particle velocities which become $\mathbf{c}$ and $\mathbf{c}_R$ in a collision that fulfills the assumptions described above. Furthermore, $\mathbf{u}_R = \mathbf{c} - \mathbf{c}_R$ is the relative velocity of two particles, V_R is the corresponding speed and parameters (s, ϵ, θ) are coordinates in a spherical

coordinate system. The nonnegative function $B(V_R,\theta)$ is the *Boltzmann collision kernel* orchestrating binary collisions, and its explicit form depends on the two-particle interaction potential. The left hand side of the Boltzmann equation is referred to as the linear transport operator, and the right hand side as the nonlinear collision operator, here denoted by $C(F)$. The collision operator presented here is rigorously valid only for repulsive potentials.

Certainly a long way has been travelled from the definition of phase space to the Boltzmann equation, and there is good reason for all these efforts. Using the mass density distribution function f, one is able to relate a mesoscopic description to a macroscopic one. Let us recall the two basic equations of macroscopic theory, namely the conservation of mass and momentum:

$$\begin{aligned} \frac{\partial \rho}{\partial t} + \nabla \cdot (\rho \mathbf{u}) &= 0, & (22) \\ -\nabla p + \nabla \cdot \vec{\boldsymbol{\tau}} &= \rho \frac{d\mathbf{u}}{dt}. & (23) \end{aligned}$$

The external force term has been omitted in Eq. (23). Because f is a mass density distribution function, the macroscopic fluid mass density can be obtained by integrating this function over its velocity argument:

$$\rho(\mathbf{r},t) = \int f(\mathbf{r},\mathbf{c},t)\ d\mathbf{c}. \tag{24}$$

Similarly one finds for the momentum density that

$$\rho(\mathbf{r},t)\mathbf{u}(\mathbf{r},t) = \int \mathbf{c}\, f(\mathbf{r},\mathbf{c},t)\ d\mathbf{c}. \tag{25}$$

Let us now present the Boltzmann equation Eq. (21) without the acceleration term, and denote the right hand side by $C(f)$. Integrating this equation over the velocity argument $\mathbf{c}$, we find that

$$\int \frac{\partial f}{\partial t} d\mathbf{c} + \int \mathbf{c} \cdot \frac{\partial f}{\partial \mathbf{r}} d\mathbf{c} = \int C(f) d\mathbf{c}. \tag{26}$$

Now the derivative in the first term on the left hand side of the equation can be taken out from the integral, and according to Eq. (24) this term gives the time derivative of the mass density. Also, the integrand in the second term on the left hand side can be expressed in the form $\nabla \cdot (\mathbf{c}f)$ because $\mathbf{c}$ does not depend on $\mathbf{r}$. Thus, after some rearranging, we find that

$$\frac{\partial \rho}{\partial t} + \int \nabla \cdot (\mathbf{c}f) d\mathbf{c} = \int C(f) d\mathbf{c}. \tag{27}$$

The divergence can be taken out of the integral on the left hand side, and using Eq. (25) we find further that

$$\frac{\partial \rho}{\partial t} + \nabla \cdot (\rho \mathbf{u}) = \int C(f) d\mathbf{c}. \tag{28}$$

We can also multiply the Boltzmann equation by $\mathbf{c}$ and integrate it then over the velocity argument. By a similar derivation as above and using the result

$$\int \mathbf{c}\,\mathbf{c}\,f \; d\mathbf{c} = \rho\,\mathbf{u}\,\mathbf{u} - \sigma_{ij}, \tag{29}$$

we finally obtain

$$-\nabla p + \nabla \cdot \vec{\boldsymbol{\tau}} = \rho \frac{d\mathbf{u}}{dt} + \int \mathbf{c}\, C(f) \; d\mathbf{c}. \tag{30}$$

In order to find the results Eqs (22) and (23), the right hand sides of Eqs (28) and (30) must vanish, and indeed this is true. Functions 1 and $\mathbf{c}$ are eigenfunctions of the integral operator $\int C(f) d\mathbf{c}$ having eigenvalue zero [1]. This property has a simple physical interpretation: mass and momentum are conserved in the collisions. This is of course obvious because these assumptions had been used already in the derivation of the Boltzmann equation. Hence

$$\begin{aligned} \frac{\partial \rho}{\partial t} + \nabla \cdot (\rho \mathbf{u}) &= 0, \\ -\nabla p + \nabla \cdot \vec{\boldsymbol{\tau}} &= \rho \frac{d\mathbf{u}}{dt}, \end{aligned} \tag{31}$$

which are the macroscopic conservation equations for mass and momentum. By a similar approach it is also possible to derive the macroscopic equation for the conservation of energy and the ideal gas law [14]. This derivation shows that the mesoscopic model constructed is compatible with a macroscopic description. There are however major advantages in the mesoscopic model. First of all Eqs (31) contain 10 unknowns (three velocity components, density and 6 components of the symmetric tensor $\vec{\boldsymbol{\tau}}$) and only 4 equations, i.e. the hydrodynamic description is not self-contained. By including the energy equation one more equation is gained but at the same time 3 more unknowns are introduced (heat flux components). To apply these equations one has to make assumptions that reduce the number of unknowns. These assumptions are always approximations and take us farther away from a realistic description of flow phenomena. If the mesoscopic model presented above is used, these assumptions are not needed. One can simply solve the Boltzmann equation and extract the information needed from the mass distribution function f. Secondly, the mesoscopic model used is applicable to infinitely high Knudsen number flows unlike e.g. the Navier-Stokes equation. One must note however that even this mesoscopic model fails if the interaction radius of molecules is not much smaller than the mean free path of the molecules, i.e. $r_\mu \ll l_m$. This restriction arises from the fact that it has been *a priori* assumed in the derivation of the Boltzmann equation that collisions are completed in a very limited domain both in space and time. As it was in the case of the Navier-Stokes equation, it is possible also in the case of the Boltzmann equation to construct a model which is valid in a wider group of fluid flow situations. These models are called generalised Boltzmann equations [15, 16]. Furthermore, numerical treatment of the Boltzmann equation is challenging due to its mathematical complexity.

3 The lattice-Boltzmann method

Historically the lattice-Boltzmann method (LBM) was developed from a similar method called the Lattice Gas Automaton (LGA). The most prominent difference between the two methods is that LGA is based on boolean variables and LBM instead on floating-point variables. In fact, the lattice-Boltzmann equation was first used as an analytical tool for computation of averages for the boolean variables in LGA. In this thesis LGA is not presented nor is the historical route to LBM. Instead an alternative route is shown, where the Boltzmann equation introduced in the preceeding section is discretised, and from this the lattice-Boltzmann equation is derived. A suitable discrete collision operator is also defined in order to arrive at an applicable computational model.

3.1 Derivation of the lattice-Boltzmann equation

In order to make the lattice-Boltzmann model amenable to computational treatment, a continuum partial differential equation (PDE) must be discretised. There are three main discretisation approaches that can be identified, namely the finite difference method (FDM), finite volume method (FVM) and finite element method (FEM), of which only the FDM is presented here [17].

The starting point of FDM is a differential form of the equation of interest. Typically these equations are conservation equations of some kind, but the method itself is applicable to any differential equation with suitable initial conditions. The computational domain is covered by a grid. At each grid point, the differential equation is approximated by replacing the partial derivatives by approximations in terms of the nodal values of the functions. This is done by using e.g. a truncated Taylor series in the following way. Let us define a function y of variables x and (time) t. The Taylor series of function y with respect to variable x can be written in the form

$$y(x_0 \pm \Delta x) = y(x_0) \pm y'(x_0)\Delta x + y''(x_0)\Delta x^2/2! \pm y'''(x_0)\Delta x^3/3! + \ldots, \quad (32)$$

For simplicity variable t is not shown. If we neglect the terms higher than first order in Δx, we find for the forward and backward differences

$$y'(x_0) = \frac{y(x_0+\Delta x)-y(x_0)}{\Delta x} \tag{33}$$

$$y'(x_0) = -\frac{y(x_0-\Delta x)-y(x_0)}{\Delta x}. \tag{34}$$

These expressions are referred to as first order because in leading order the error term is $O(\Delta x)$. By summing up the forward and backward difference expressions above we find that

$$y'(x_0) = \frac{y(x_0+\Delta x)-y(x_0-\Delta x)}{2\Delta x} \tag{35}$$

is second order accurate since in leading order the error term is $O(\Delta x^2)$. Equation (35) is called the central difference. One can also sum up the second order forward and backward forms of the truncated Taylor series so as to find a second differential for function y,

$$y''(x_0) = -\frac{y(x_0+\Delta x)-2y(x_0)+y(x_0-\Delta x)}{\Delta x^2}. \tag{36}$$

The rate of change of function y with time t can also be determined with a similar way, and the result is

$$\frac{\partial y}{\partial t} = \frac{y(x_0,t+\Delta t)-y(x_0,t)}{\Delta t}. \tag{37}$$

Now if the flow relationship is known then the conditions at one time step in the future can be calculated from their known values at nodes at the current time step. If this kind of direct calculation is possible, the method is referred to as explicit, otherwise it is implicit.

The first step in the path towards the lattice-Boltzmann equation (LBE) is discretisation of the Boltzmann equation Eq. (21). The most usual way to do

this is to allow particles of the system to have only certain velocities that form a velocity set $\Psi_q = \{\mathbf{c}_0, \mathbf{c}_1, \ldots, \mathbf{c}_{q-1}\}$. Here the amount of possible velocities is denoted by q. Using this restriction the discrete Boltzmann equation can be expressed in the form

$$\frac{\partial f_i}{\partial t} + \mathbf{c}_i \cdot \frac{\partial f_i}{\partial \mathbf{r}} + \mathbf{a} \cdot \frac{\partial f_i}{\partial \mathbf{c}_i} = C_i(\vec{f}), \qquad i = 0, 1, \ldots, q-1, \tag{38}$$

where $f_i = f(\mathbf{r}, \mathbf{c}_i, t)$ and $\vec{f} = (f_0, f_1, \ldots, f_{q-1})$. The continuous binary collision operator $C(f)$ is replaced by a discrete counterpart $C_i(\vec{f})$. Although discretisation is necessary for acquiring an equation amenable to numerical treatment, there are also significant benefits in this form of the Boltzmann equation. The mass density distribution function f in the original Boltzmann equation depends on seven independent variables while its discrete counterpart f_i is a function of only 4 independent variables. Furthermore, the collision operator in the original equation involves integrals while in the discrete version it is an operator that involves summations.

Let us now consider for simplicity the discrete Boltzmann equation without the external acceleration term,

$$\frac{\partial f_i}{\partial t} + \mathbf{c}_i \cdot \frac{\partial f_i}{\partial \mathbf{r}} = C_i(\vec{f}), \qquad i = 0, 1, \ldots, q-1. \tag{39}$$

We can use the finite difference method introduced above to discretise the remaining derivative terms. The first term on the left hand side is the time derivative of the discretised mass density distribution funtion, and its first order forward difference is given by

$$\frac{\partial f_i}{\partial t} = \frac{f_i(\mathbf{r}, t + \Delta t) - f_i(\mathbf{r}, t)}{\Delta t}. \tag{40}$$

Let us now rearrange Eq. (39) in a way that only the time derivative is on the left hand side of the equation,

$$\frac{f_i(\mathbf{r},t+\Delta t)-f_i(\mathbf{r},t)}{\Delta t} = -\mathbf{c}_i \cdot \frac{\partial f_i(\mathbf{r},t)}{\partial \mathbf{r}} + C_i(\mathbf{r},t), \qquad i = 0,1,\ldots,q-1. \quad (41)$$

The right-hand side is now subjected to an upwind treatment, i.e. the two terms on the right hand side are both evaluated at location $(\mathbf{r}-\Delta t\mathbf{c}_i)$:

$$\frac{f_i(\mathbf{r},t+\Delta t)-f_i(\mathbf{r},t)}{\Delta t} = -\mathbf{c}_i \cdot \frac{\partial f_i(\mathbf{r}-\Delta t\mathbf{c}_i,t)}{\partial \mathbf{r}} + C_i(\mathbf{r}-\Delta t\mathbf{c}_i,t). \quad (42)$$

By applying the result for the first order forward difference from above, we find that

$$\mathbf{c}_i \cdot \frac{\partial f_i(\mathbf{r}-\Delta t\mathbf{c}_i,t)}{\partial \mathbf{r}} = \frac{f_i(\mathbf{r},t)-f_i(\mathbf{r}-\Delta t\mathbf{c}_i,t)}{\Delta t}. \quad (43)$$

By substituting this result in Eq. (42) we arrive at the expression

$$\frac{f_i(\mathbf{r},t+\Delta t)-f_i(\mathbf{r},t)}{\Delta t} = \frac{f_i(\mathbf{r}-\Delta t\mathbf{c}_i,t)-f_i(\mathbf{r},t)}{\Delta t} + C_i(\mathbf{r}-\Delta t\mathbf{c}_i,t). \quad (44)$$

Next we multiply this equation by Δt, formally replace $\mathbf{r}$ by $\mathbf{r}+\Delta t\mathbf{c}_i$ and re-arrange terms:

$$f_i(\mathbf{r}+\Delta t\mathbf{c}_i,t+\Delta t) = f_i(\mathbf{r},t)+\Omega_i(\mathbf{r},t). \quad (45)$$

In the above equation the term $\Delta t C_i$ has been identified with the collision operator Ω_i, and the resulting expression is known as the lattice-Boltzmann equation. Discretised counterparts of Eqs (24) and (25) can now be expressed in the form

$$\rho(\mathbf{r},t) = \sum_i f_i(\mathbf{r},t), \quad (46)$$

$$\rho(\mathbf{r},t)\mathbf{u}(\mathbf{r},t) = \sum_i \mathbf{c} f_i(\mathbf{r},t), \quad (47)$$

and the model is made amenable to numerical treatment when we specify a particular collision operator. A wide variety of collision operators and lattice-Boltzmann stencils can be chosen so as to arrive at specific lattice-Boltzmann models.

3.2 Lattice-Boltzmann models

The collision operator in Eq. (45) can be modelled with many different methods. The most usual approach is to model the collision operator by relaxing the distribution function f towards its equilibrium value. The simplest and very widely used relaxation model is the single relaxation time lattice BGK model (LBGK), which expresses the evolution equation in the form [18]

$$f_i(\mathbf{r}+\Delta t\mathbf{c}_i, t+\Delta t) = f_i(\mathbf{r},t) - \omega\left(f_i(\mathbf{r},t) - f_i^{eq}(\mathbf{r},t)\right). \tag{48}$$

The name of the model comes from the fact that the relaxation rate of the system is controlled by a single parameter ω. It can also be shown that parameter ω has direct connection to the kinematic viscosity of the fluid,

$$\nu = \frac{1}{6}\left(\frac{2}{\omega} - 1\right). \tag{49}$$

From a physical perspective it can now be seen that parameter ω must satisfy the condition $0 < \omega < 2$, otherwise the viscosity attains nonpositive values. The discrete equilibrium function can be obtained from the Maxwell-Boltzmann distribution [19]

$$f^{eq} = \rho\left(\frac{m}{2\pi k_b T}\right)^{3/2} exp\left(\frac{-m(\mathbf{c}-\mathbf{u})^2}{2k_b T}\right), \tag{50}$$

where $\mathbf{c}$ is the particle velocity and $\mathbf{u}$ is the macroscopic fluid flow velocity. When the velocity space is discretised and Taylor expansion is used, one finds for the discrete equilibrium function [20]

$$f_i^{eq} = \rho(\mathbf{r},t)w_i\left(1+\frac{\mathbf{c}_i\cdot\mathbf{u}}{c_s^2}+\frac{(\mathbf{c}_i\cdot\mathbf{u})^2}{c_s^4}-\frac{u^2}{2c_s^4}\right), \tag{51}$$

where subscript i refers to the discrete velocity $\mathbf{c}_i$, w_i are lattice dependent weight factors and c_s is the speed of sound of the lattice. The construction of a specific model is still far from finished. The discrete velocities, which are closely related to the spatial grid chosen, must be specified. The velocity sets are constructed in a n-dimensional regular lattice with m velocities (denoted by $DnQm$). For example, the $D3Q19$ model is constructed on a three dimensional cubic lattice and has 19 discrete velocities (see Fig. 2). Other commonly used models are $D1Q3$, $D2Q9$, and $D3Q15$ [21] and models with signicantly higher number of velocities ($D1Q5$, $D2Q25$ and $D3Q125$) have also been constructed [22].

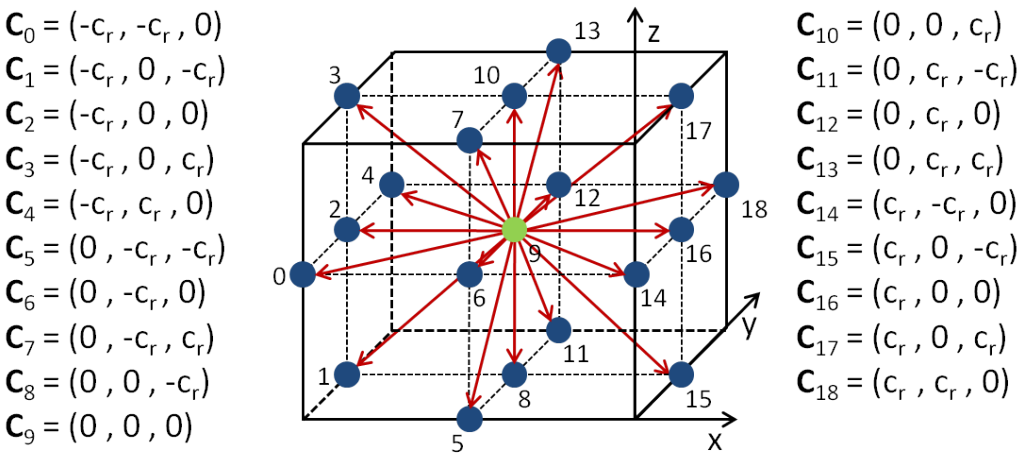

Figure 2: Nodal points and velocity vectors used in the $D3Q19$ model. There are 18 velocities of nonzero magnitude and one rest velocity of zero magnitude. Three different speeds are included in this model, namely 0, c_r and $\sqrt{2}c_r$. The reference speed c_r is connected to the lattice spacing and discrete time step through $\Delta r = \Delta t c_r$.

After choosing the spatial grid and velocities, one must define the weight factors w_i in order to obtain an applicable numerical model. The factors related to equal

speeds are the same and therefore there are three different factors in the $D3Q19$ model. The w_i's are determined so as to achieve isotropy of the fourth-order tensor of velocities and Galilean invariance [18]. With these restrictions one finds $w_0 = 1/3$ for the rest velocity, $w_1 = 1/18$ for the nearest neighbours and $w_2 = 1/36$ for the second nearest neighbours in the $D3Q19$ model.

The model presented above is the one used in the simulation part of this thesis. It is however worth mentioning that other models than LBGK do exist. In two-relaxation-time (TRT) models any pair of populations with opposite velocities $(\mathbf{c}_i, \mathbf{c}_{i'})$ can be decomposed into its symmetric (even) and anti-symmetric (odd) components [23]:

$$f_i = f_i^+ + f_i^-, \qquad f_i^+ = \frac{1}{2}(f_i + f_{i'}), \qquad f_i^- = \frac{1}{2}(f_i - f_{i'}), \qquad \mathbf{c}_i = -\mathbf{c}_{i'}. \tag{52}$$

Odd moments of the symmetric function and even moments of the antisymmetric function vanish, and, with the above definitions, the LB equation can be expressed in the form

$$\begin{aligned} f_i(\mathbf{r} + \Delta t\mathbf{c}_i, t + \Delta t) &= f_i(\mathbf{r}, t) - \omega_e f_i^{+,neq}(\mathbf{r}, t) - \omega_o f_i^{-,neq}(\mathbf{r}, t) \\ &= f_i(\mathbf{r}, t) - \frac{1}{2}(\omega_e + \omega_o) f_i^{neq}(\mathbf{r}, t) - \frac{1}{2}(\omega_e - \omega_o) f_{i'}^{neq}(\mathbf{r}, t), \end{aligned} \tag{53}$$

where ω_e and ω_o are relaxation parameters and $f_i^{neq} = f_i - f_i^{eq}$. Although the TRT model is a little bit more difficult to implement and computationally more expensive than the BGK model, parameter ω_o provides an additional degree of freedom. Usually it is adjusted so as to minimise the nonphysical viscosity-dependent slip-velocity that appears in LBM [24]. Parameter ω_e controls the viscosity in the same way as in the BGK model. Even more relaxation parameters can be used in the so called multi-relaxation-time (MRT) models. These models provide more degrees of freedom in terms of an increasing number of simulation parameters. Obviously computational requirements also increase. Introduction of MRT models is omitted here, but details can be found for example in Refs [25], [26] and [27].

Above, some lattice-Boltzmann models were introduced. These models express the time development of the discretised distribution functions f_i; and hydrodynamic variables are moments of f_i, see Eqs (46) and (47). An essential question is what macroscopic equations these simplified and discretised models approximate. By using the Chapman-Enskog analysis, it can be shown that the LBGK model conforms to the equation of conservation of mass and the Navier-Stokes equation. The analysis is somewhat laborious and is beyond the scope of this thesis, but details can be found e.g. from Ref. [20]. To summarize, Fig. 3 shows a schematic description of the main steps that lead to LB models.

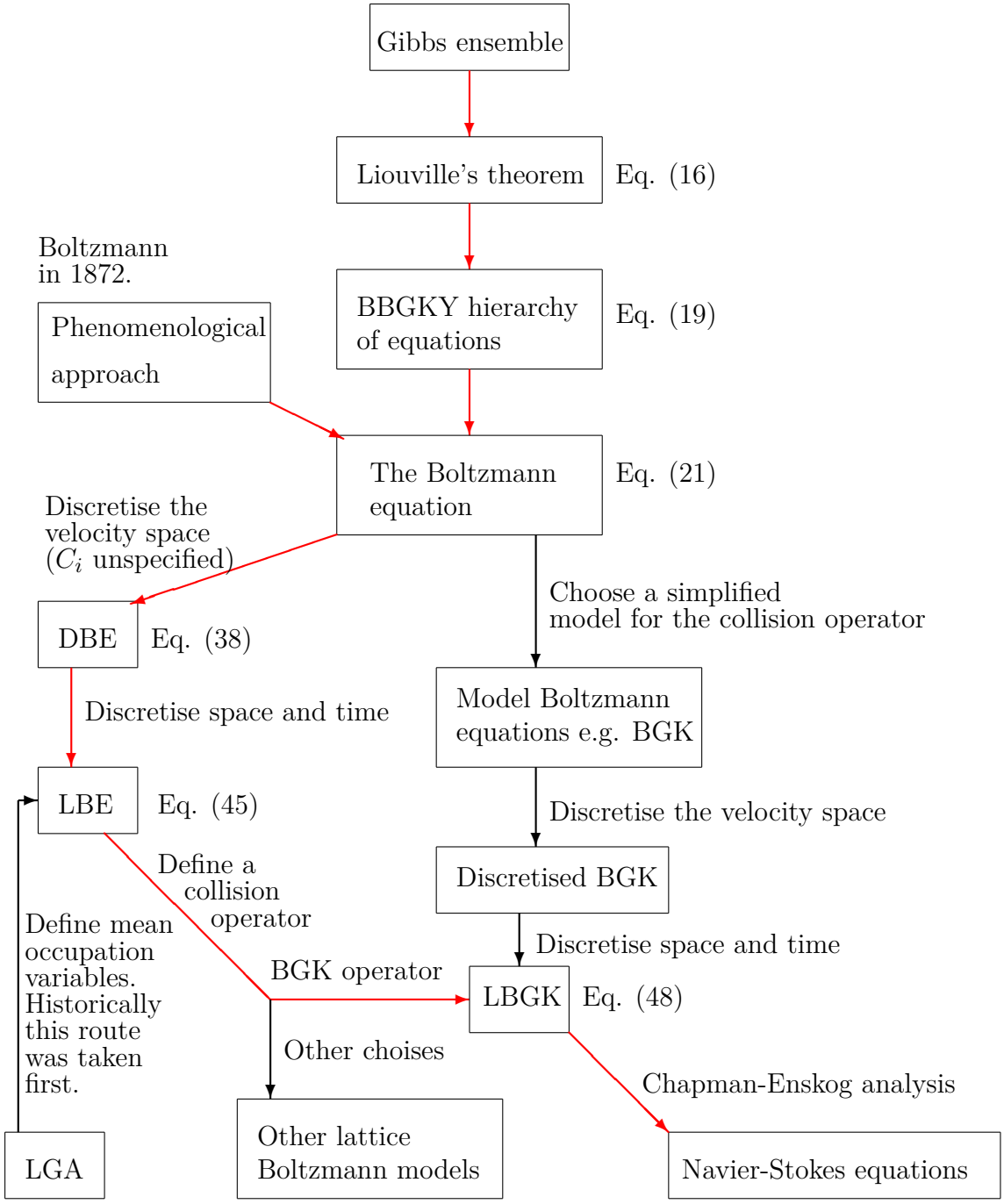

Figure 3: Paths leading to the LBGK model. Red arrows present the path followed in this thesis and black arrows present alternative routes. Some of the essential equations are also shown.

3.3 Boundary conditions and simulation geometries

Boundary conditions must be specified at domain boundaries and fluid-solid interfaces. To state whether the node is solid or fluid, only one data structure has to be added to the model. This structure indicates the state of each node: e.g., 0 for fluid and 1 for solid. After this division into fluid and solid nodes has been done, we need to implement the update rules which define the way the distribution functions behave when a boundary between the two is encountered. Probably the most widely used update rule is the halfway bounce-back boundary condition which models the no-slip condition inherent in real life fluid flows. The idea is to simply reflect the distribution functions which would otherwise end up inside the solid nodes in the streaming step. The condition is presented in detail in Fig. 4

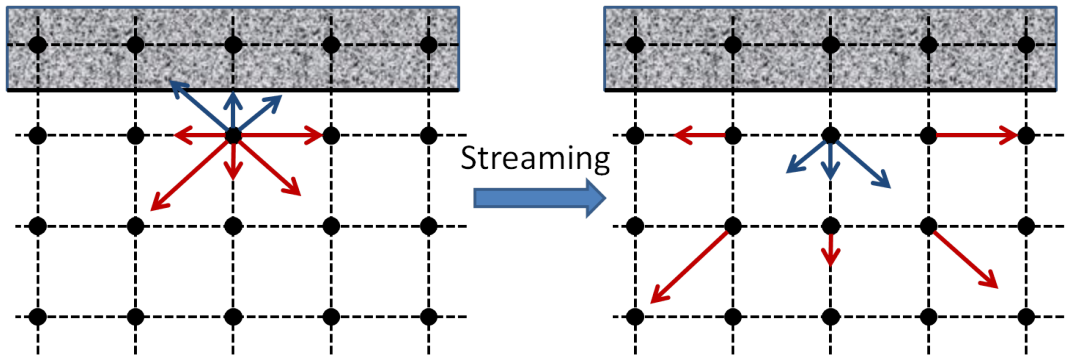

Figure 4: Halfway bounce-back boundary condition in a two dimensional lattice. Blue arrows represent the components of mass density distribution function that are reflected and the red ones are not affected by the boundary condition. The lengths of the arrows indicate the relative magnitude of the components.

The name "halfway" comes from the effective location of the reflection. The solid boundary lies halfway between the adjacent fluid and solid nodes, and reflection takes place during one time step. The halfway bounce-back is used in the simulations of this thesis, but a wide variety of other fluid-solid boundary conditions exist, for example halfway bounce-forward, fullway bounce-back and fullway bounce-forward to name a few. The halfway bounce-forward is sim-

ilar to the method presented above, but it differs in the way the distribution functions are reflected. The reflection happens only in the direction normal to the boundary, not parallel to it, thus allowing the fluid to "slip". The fullway bounce-back and fullway bounce-forward are similar, but in these models the boundary lies exactly in the location of the solid node, and reflection takes place during two consecutive time steps. A more detailed description of fluid-solid boundary conditions can be found in Ref. [2].

In addition to the boundary conditions between fluid and solid, conditions for grid boundaries must also be implemented. One option is to use periodic boundary conditions. The idea is to translate the components of the mass density distribution function, which cross the grid boundaries, to the other side of the grid. Fig. 5 illustrates this condition.

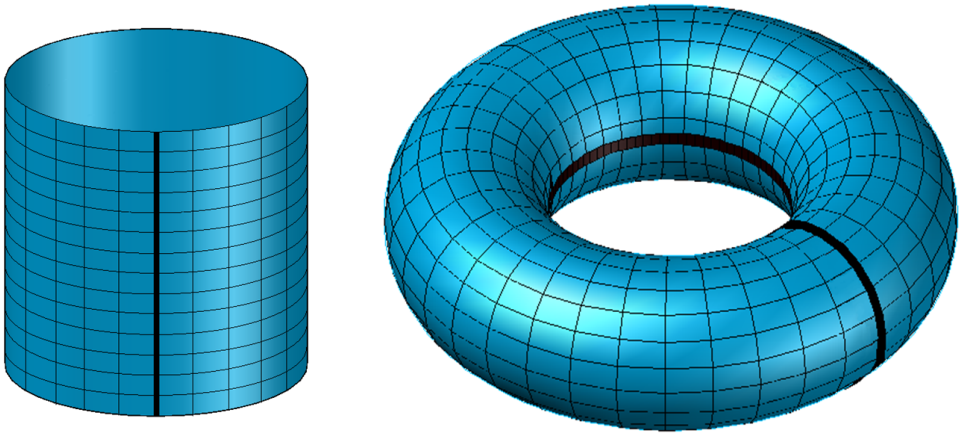

Figure 5: Presentation of periodic boundary conditions in a two dimensional lattice. On the left periodicity is applied in one coordinate direction and on the right in two directions. The thick black lines denote the boundaries of the lattice, and the periodic boundary condition is applied over these boundaries.

Another boundary condition used also in our simulations is the constant velocity boundary condition. The idea of this boundary method is to prescribe velocity and density at the boundary, and calculate from these values the unknown components of the distribution function. Obviously the components

which came from inside the computational domain are known. For example, if we consider Fig. 2 and suppose that the boundary lies in the zy-plane and the positive x-direction is directed towards the computational domain, the unknown components of the distribution function after streaming are f_{14}, f_{15}, f_{16}, f_{17} and f_{18}. To assign values to these unknown components we assume bounce-back of the non-equilibrium part which can be stated as

$$
\begin{aligned}
f_{14} &= f_{14}^{eq} + f_4^{neq} = f_{14}^{eq} + f_4 - f_4^{eq} && (54)\\
f_{15} &= f_{15}^{eq} + f_3^{neq} = f_{15}^{eq} + f_3 - f_3^{eq} && (55)\\
f_{16} &= f_{16}^{eq} + f_2^{neq} = f_{16}^{eq} + f_2 - f_2^{eq} && (56)\\
f_{17} &= f_{17}^{eq} + f_1^{neq} = f_{17}^{eq} + f_1 - f_1^{eq} && (57)\\
f_{18} &= f_{18}^{eq} + f_0^{neq} = f_{18}^{eq} + f_0 - f_0^{eq}. && (58)
\end{aligned}
$$

Now, using the equilibrium distribution function Eq. (51), one can solve the unknown components via a straightforward calculation. In the calculations the appropriate weight factors and speed of sound for the lattice are used. For D3Q19 these are $w_0 = 1/3$, $w_1 = 1/18$, $w_2 = 1/36$ and $c_s^2 = c_r^2/3$. For example the calculation of component 14 starting from Eq. (54) preceeds such that

$$
\begin{aligned}
f_{14} &= f_4^{neq} + f_{14}^{eq} = f_4 - f_4^{eq} + f_{14}^{eq}\\
&= f_4 - \frac{\rho}{36}\left(1 + \frac{u_y c_r - u_x c_r}{c_r^2/3} + \frac{(u_y c_r - u_x c_r)^2}{c_r^4/9} - \frac{(u_x^2 + u_y^2)}{2c_r^2/3}\right)\\
&+ \frac{\rho}{36}\left(1 + \frac{u_x c_r - u_y c_r}{c_r^2/3} + \frac{(u_x c_r - u_y c_r)^2}{c_r^4/9} - \frac{(u_x^2 + u_y^2)}{2c_r^2/3}\right)\\
&= f_4 + \frac{\rho}{12}\frac{u_x c_r - u_y c_r}{c_r^2} + \frac{\rho}{12}\frac{u_x c_r - u_y c_r}{c_r^2}\\
&= f_4 + \rho\frac{u_x - u_y}{6c_r}. && (59)
\end{aligned}
$$

As is evident, most of the terms vanish and we are left with a simple expression for f_{14}. Similar calculations can be done also for Eqs (55)-(58), which give a group of expressions for all the initially unknown components. These expressions are

$$f_{14} = f_4 + \rho\frac{u_x - u_y}{6c_r}, \qquad f_{15} = f_3 + \rho\frac{u_x - u_z}{6c_r}, \qquad f_{16} = f_2 + 2\rho\frac{u_x}{6c_r}$$
$$f_{17} = f_1 + \rho\frac{u_x + u_z}{6c_r}, \qquad f_{18} = f_0 + \rho\frac{u_x + u_y}{6c_r}. \tag{60}$$

Now we should check that these expressions enforce the correct hydrodynamic variables, for example density ρ and momentum densities ρu_x, ρu_y and ρu_z. Density can be calculated using Eq. (46) together with the calculated values for initially unknown components Eq. (60),

$$\begin{aligned}
\sum_{i=0}^{18} f_i &= \sum_{i=0}^{13} f_i + f_4 + \rho\frac{u_x - u_y}{6c_r} + f_3 + \rho\frac{u_x - u_z}{6c_r} \\
&\qquad + f_2 + \frac{2\rho u_x}{6c_r} + f_1 + \rho\frac{u_x + u_z}{6c_r} + f_0 + \rho\frac{u_x + u_y}{6c_r} \\
&= 2\sum_{i=0}^{4} f_i + \sum_{i=5}^{13} f_i + 6\rho\frac{u_x}{6c_r} + \rho\frac{u_y - u_y}{6c_r} + \rho\frac{u_z - u_z}{6c_r} \\
&= 2\sum_{i=0}^{4} f_i + \sum_{i=5}^{13} f_i + \rho\frac{u_x}{c_r} \\
&= 2\sum_{i=0}^{4} f_i + \sum_{i=5}^{13} f_i + \sum_{i=14}^{18} f_i - \sum_{i=0}^{4} f_i \\
&= \sum_{i=0}^{18} f_i = \rho
\end{aligned} \tag{61}$$

Thus, the correct density is attained. Similarly one can calculate the first order moments i.e. momentum densities in different coordinate directions, and find that

$$\sum_i c_{ix} f_i = \rho u_x, \tag{62}$$
$$\sum_i c_{iy} f_i = c_r\left(f_{11} + f_{12} + f_{13} - f_5 - f_6 - f_7 + \rho\frac{u_y}{3c_r}\right) \neq \rho u_y, \tag{63}$$
$$\sum_i c_{iz} f_i = c_r\left(f_7 + f_{10} + f_{13} - f_5 - f_8 - f_{11} + \rho\frac{u_z}{3c_r}\right) \neq \rho u_z. \tag{64}$$

It is evident that the only direction in which the prescribed components of distribution function enforce the correct momentum density is the direction normal to the boundary. Therefore more elaborate conditions for the unknown components must be assigned to correct for this discrepancy. Indeed, boundary schemes which enforce zeroth and first order and even higher order moments can be constructed. Actually, the scheme used in our simulations uses a boundary scheme which enforces seven hydrodynamic moments (density, momentum density in every coordinate direction and three second order moments related to the viscous stresses). These higher order schemes are not presented here, but more information can be found in Ref. [20].

In our simulations, the complex flow domains, or geometries, are represented by digital images acquired with two different methods, namely confocal microscopy and x-ray tomography. Confocal microscopy allows us to see the actual geometry of the paper and also the attached ink particles. This gives us the possibility to compare results of simulations with the actual locations of ink particle attachment. The sensitivity of confocal microscopy decreases however with increasing distance from paper surface, and this should be taken into account when analysing the results. X-ray tomography does not suffer from this limitation, but with this method the ink distribution cannot be seen. Nevertheless, when images of the sample geometry were acquired, they were in greyscale form, and were then binarised so as to provide the simulation geometries. In Fig. 6 an original confogal microscopy image and its binarised form are shown.

For binarizing an image, different algorithms can be used. A simple approach is to choose a threshold value which is used to determine which voxels are black and which white. Choosing of this threshold value can be based on various methods. In the present work the threshold value was chosen manually based on visual inspection, and the binarised image was processed further with the despeckle algorithm.

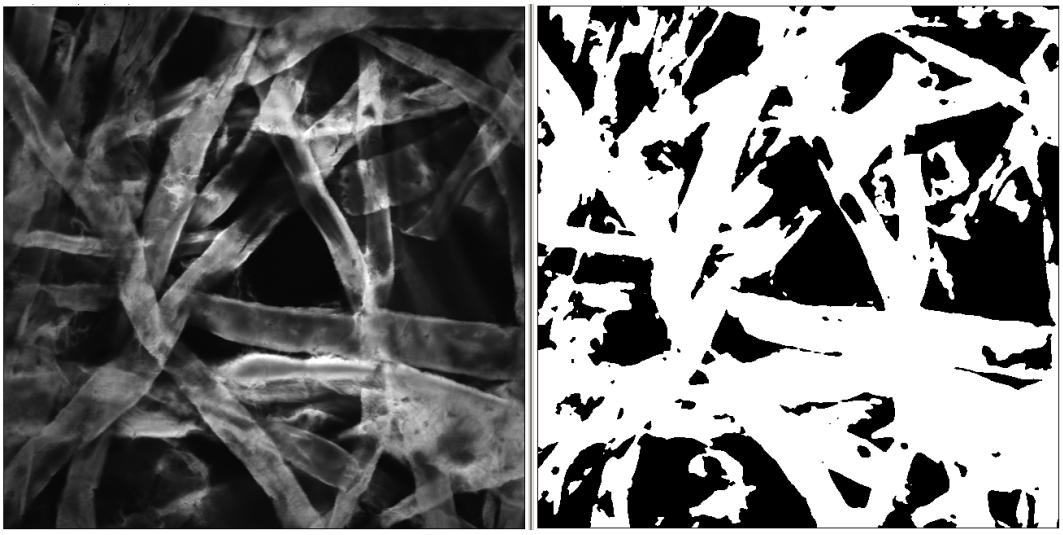

Figure 6: A confogal microscopy image of a sample of paper and its binary form.

4 Simulating fluid-particle suspensions

The LBGK model introduced in the previous section with suitable boundary and initial conditions is readily amenable to numerical computation, but is not sufficient for the goals of this thesis. The model must be connected to another model that describes the dynamical behaviour of ink particles moving in a flow field. This section describes the particle model and the velocity-verlet algorithm used to discretise the model. Also, some restrictions of the model are discussed.

4.1 Mathematical model for particle dynamics

In order to simulate the movement of ink particles in a flow field, the LBGK model introduced in the previous section must be extended so as to incorporate particle dynamics. In practice this is done by using a form of the Basset-Bousinnesq-Oseen equation [28]

$$m\mathbf{a} = mC_f(\mathbf{u}-\mathbf{v}) + C_d\mathbf{R} + \mathbf{F}_{pp}, \tag{65}$$

which is basically Newton's second law of motion for a particle. Here m, $\mathbf{a}$ and $\mathbf{v}$ are particle's mass, acceleration and velocity, respectively. The three terms on the right hand side of Eq. (65) are, in the order from left to right, the convective force, the random diffusion force and force between adjacent particles. Coefficients C_f and C_d are simulation parameters used to control the magnitudes of convective and diffusive forces, and $\mathbf{R}$ is a three component random term with components having zero mean and unit variance. The particle description is connected explicitly with the LBGK model through the convective term, in which fluid velocity $\mathbf{u}$ is interpolated from its values at adjacent lattice points given by the LBGK simulation to the center of the particle. Even though the diffusive term appears to have no connection with the fluid flow, it is connected on physical grounds, i.e. via Brownian motion. So the total force applied to the particle by the fluid consists of convective and diffusive forces. In accordance with the Newton's third law, a force applied by the particle to the fluid is equal in magnitude, but opposite in direction to the force excerted by the fluid to the particle. This force is then distributed over the neighbouring lattice nodes representing the fluid. The particle-particle force F_{pp} in Eq. (65) is calculated over particles which lie in the neighbouring lattice cells, and the force between two particles can be expressed in the form

$$\mathbf{F_{pp}^{ji}} = -C_{pp} d^{-4} (\mathbf{r}_j - \mathbf{r}_i)/d_{cent}. \tag{66}$$

Here C_{pp} is a simulation parameter, d is the distance between the surfaces of particles i and j, $\mathbf{r}_i$ the location of particle i and d_{cent} is the distance between the centres of particles i and j.

4.2 Velocity Verlet algorithm

The simple model describing particle dynamics Eq. (65) can be discretised using the velocity Verlet algorithm which consists of three equations for updating particle's position, velocity and applied force:

$$\mathbf{r}(t+\Delta t) = \mathbf{r}(t) + \mathbf{v}(t)\Delta t + (1/2)\mathbf{F}(t)\Delta t^2/m \tag{67}$$

$$\mathbf{F}(t+\Delta t) = \mathbf{F}_{new}. \tag{68}$$

$$\mathbf{v}(t+\Delta t) = \mathbf{v}(t) + (1/2)(\mathbf{F}(t) + \mathbf{F}_{new})\Delta t/m. \tag{69}$$

If one knows particle's position, velocity and force applied to it at time t, the above equations can be used successively to find their values at a future time $t+\Delta t$. The term $\mathbf{F}_{new}$ can be calculated from Eq. (65). In principle these equations can now be used with Eqs (65) and (66) to simulate particle's trajectory in time and space. In practical simulations however the situation is not so simple. Particles can come close to each other or walls of the simulation geometry and in many of these situations the dynamics must be constricted for computational and physical reasons. The constriction rules implemented in our model are presented in the next section.

4.3 Wall attachment and particle restrictions

As a particle moves in the simulation geometry it can encounter three kinds of obstacles, namely solid nodes, boundaries of the computational domain and other particles. Obviously the considered particle is affected by these encounters so that its movement is altered. Sometimes its movement is nonphysical in nature or produces conditions problematic for the computational implementation. In these situations the dynamics are restricted, mostly in a heuristic manner.

Let us first consider the case where the particle comes close to a solid node. If the particle's position after the update step, Eq. (67), lies inside a solid node, the displacement is halved and another attempt is made. Ten successive halving attemps are made and if the update still brings the particle inside the solid node, the update is rejected. In this way the unphysical effect of particles appearing inside the solid is avoided. When the particle comes in close approximity to the wall, attachment can also occur. The probability for this process depends on the number of solid walls around the particle, the distance d to these walls

and the wall attachment coefficient λ_a which is given as a simulation parameter. The function giving this probability can be expressed in the form

$$p = w_i \cdot exp\left(\frac{-d}{\lambda_a}\right), \tag{70}$$

where w_i is a weight factor which depends on the distance of the particle cell from the solid cell. Three different values are used: $w_1 = 16/61$ for cells with common faces, $w_2 = 4/61$ for cells with common edges and $w_3 = 1/61$ for cells with common vertices (see Fig. 7). The probability function Eq. (70) is summed over all solid cells around the cell containing the particle so as to find the total probability for attachment. If this value is higher than a random reference probability, attachment will take place and the particle will be stopped at its current position. A certain amount of particles can be attached to the same cell, but when a threshold number is exceeded, the cell is turned into solid, i.e. it is sedimented.

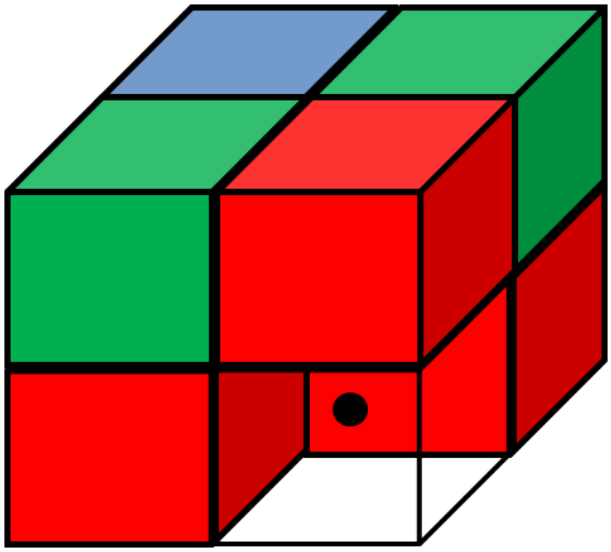

Figure 7: Illustration of cells affecting the attachment probability. The attaching particle is in the transparent cell and red, green and blue cells correspond to weight factors $w_1 = 16/61$, $w_2 = 4/61$ and $w_3 = 1/61$, respectively.

The simulation geometry is finite, and sometimes particles cross the domain

boundaries. If the boundary which is crossed is in the main flow direction, such particles are removed from the simulation. This happens often in the beginning of the simulation, when particles are initialized too close to the boundaries and diffusion drives them across. In this case we do not actually contrict the dynamics of the particles, we simply allow them to wonder away from the simulation geometry.

Particle-particle collisions and motion of particles are restricted in many ways. Particles affect each other through Eq. (66), but in order to keep the forces finite, the particle-particle force assumes a certain value at small distances. Even with this restriction, the total force applied by all surrounding particles can grow above a predefined maximum value which then replaces the actual force. Besides particle-particle forces, also fluid-particle forces are constricted. When direct calculation of the force applied by the fluid to the particle as given by the first two terms in Eq. (65) gives a value above a certain limit, the actual value is replaced by the predefined maximum fluid-particle force. In a similar way, particle's speed and displacement are restricted to be within the corresponding maximum values so as to avoid, for example, instances where particles jump over one or several nodes. These events could be tricky without restrictions because then particles could unphysically jump over solid nodes or, in parallel systems, cause problems in the border regions between two processes. Every time one of these restrictions occur, the dynamics are not properly executed. Thus, simulations should be optimised so as to produce as few restrictions as possible.

5 Simulations

In this study the method introduced above was used to simulate movement of ink particles and their attachment to paper. Two different imaging techniques were used to acquire the geometry of the simulations, namely confocal microscopy and X-ray tomography. With confocal microscope also the ink could be observed, and its distribution could then be compared to that found by simulations. With X-ray tomography the ink could not be seen, but more realistic

simulation geometries could be acquired.

As the simulation advanced, particles were attached to the simulation geometry according to the rules described in the previous section. After the simulation, the locations of attached particles could be read from a text file. For visualisation reasons and to make use of the small particle number compared to that in an experimental situation, the attached particles were visualised according to the colouring scheme presented in Fig. 8.

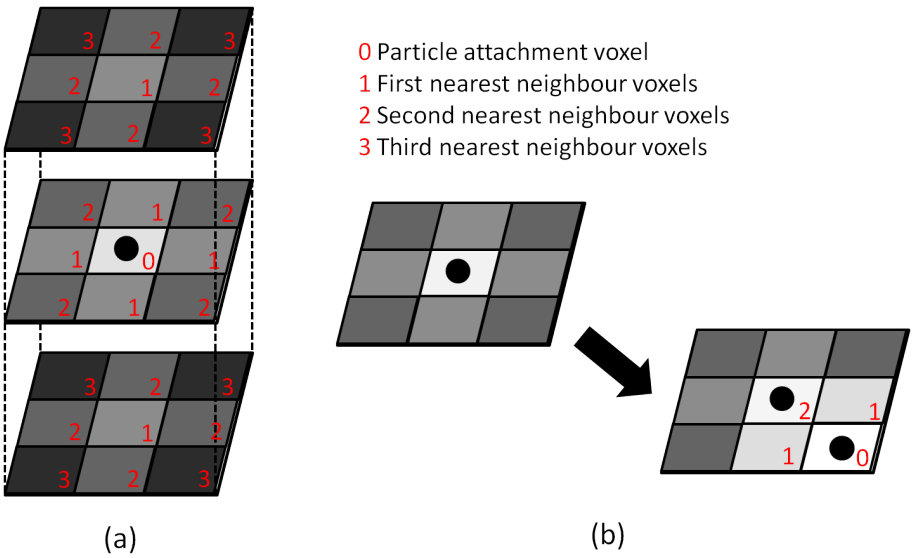

Figure 8: Colouring scheme for particles. In (a) a particle is attached to a location where all neighbours are initially uncoloured and in (b) a particle is attached close to another particle. In (b) only one layer is shown for clarity.

Each attached particle affects the voxel to which it is attached, and also its 26 neighbouring voxels. The voxel where particle is attached gets the brightest colour, the first nearest neighbour voxels get the second brightest colour and so on. With this colouring method simulations produce a more natural overall coloring of the ink pigments coloured regions by allowing intermediate brightness levels between black and white.

5.1 Simulations in confocal microscopy images

A series of simulations with different simulation parameters were done for a paper sample with no surface or bulk sizing to reduce any chemical effects of ink attachment. A result from a single simulation is shown in Fig. 9 with a corresponding experimental result. These images display similarities as well as differencies. It is evident from both images that ink tends to move along with the fluid flow, thereby large amounts of ink can be found near the largest flow channels. Differencies on the other hand can be observed in the distribution of ink as a function of distance from paper surface. There can be many reasons for this discrepancy. First of all, the actual paper structure contained a lot of fine matter which disappears when the image is binarised. Ink propagation is however affected by this fine matter. Secondly, and probably most importantly, the confogal microscopy image shows only a fraction of the full thickness of the paper, and therefore the simulation is in fact done only for a thin surface layer in contrast with the experimental result that is for the whole paper thickness. A thin simulation geometry introduces flow channels which are not really there in the actual sample, and therefore particles flow more easily through and are not attached in the paper. This effect is probably the reason why the attached ink looks quite different in the simulated and experimental results of Fig. 9.

It is evident from cross sections taken at varying distance from paper surface (Fig. 10) that the simulated and experimental results differ more in the deeper layers of paper, which supports the hypothesis that a thin simulation geometry is partly responsible for the observed discrepancies between simulations and experiments.

A quantitative comparison between simulated and experimental results was done by determining the ink density as a function of distance from paper surface. We found that the density profile in both cases follows a double exponential form,

$$f(x) = A_1 * e^{-x/t_1} + A_2 * e^{-x/t_2}, \tag{71}$$

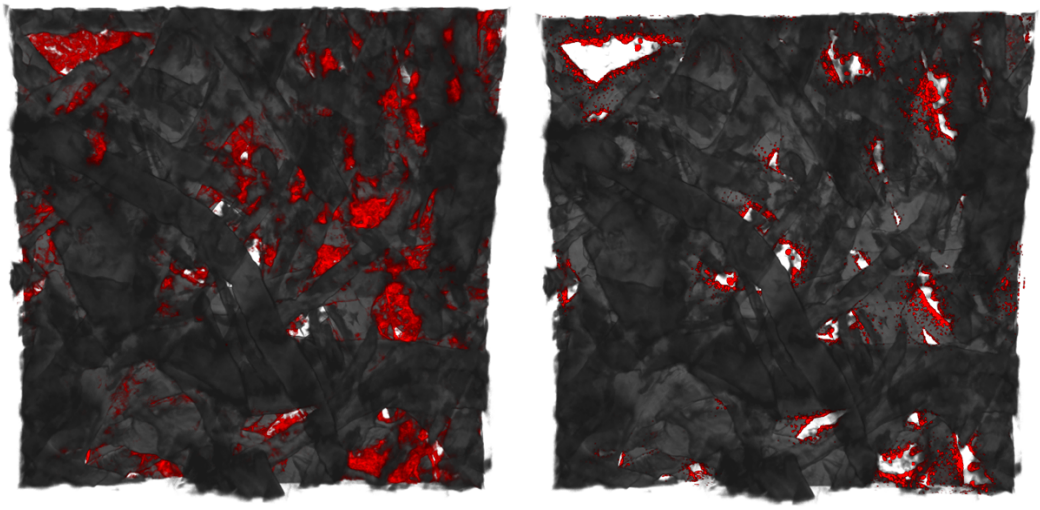

Figure 9: On the left, bottom view of a surface layer of a paper sample with ink as recorded by confocal microscopy. On the right, the corresponding simulation result.

as demonstrated in Fig 11.

We concluded that these two terms are related to two different processes that take place in paper. The exponential term with a smaller decay parameter t_1 accounts for surface layer effects while the other term with parameter t_2 is related to particles convected deeper in the paper structure. Parameters of the fit were used to compare the results with those of the simulations. Because in the simulations the particle intensity was much lower than in the experimentas, comparison was done with a normalised form of Eq. (71),

$$f(x) = \frac{1}{A_1 * t_1 + A_2 * t_2} * (A_1 * e^{-x/t_1} + A_2 * e^{-x/t_2}). \tag{72}$$

In all the simulations the surface layer effect was relatively stronger than in the experiments as is evident from Figs 12-15 and the fitting parameters in Table 1. The probable reasons for this were given already above.

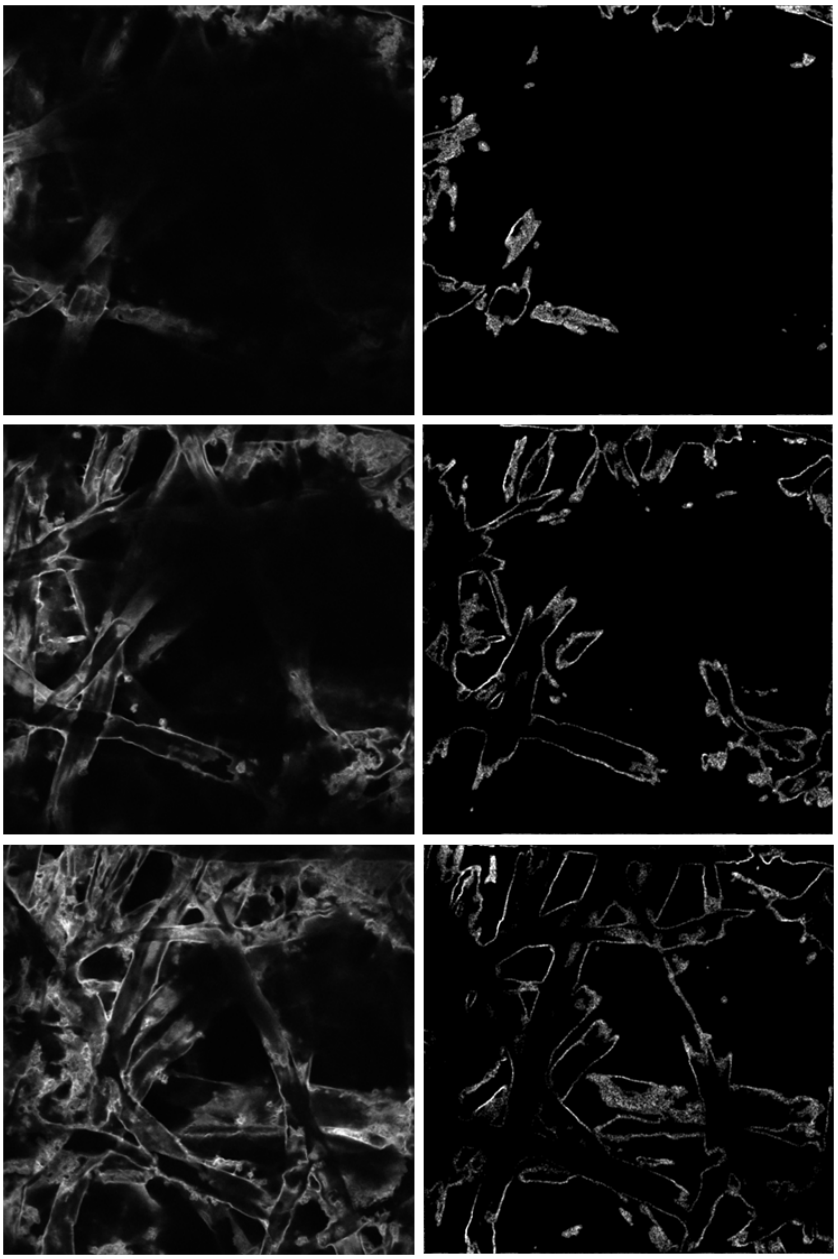

Figure 10: Cross sections of a paper sample at varying distance from paper surface. On the left, images of experimental results are shown and on the right are the corresponding simulation results. Distance from paper surface increases from top to bottom.

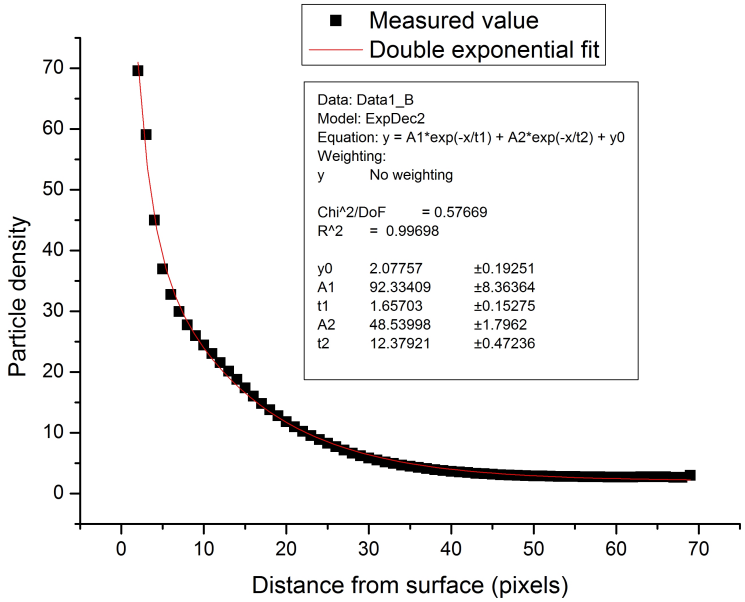

Figure 11: An ink density profile determined from a confogal microscopy image. A double exponential function was used for fitting the data, and the fitting parameters are also shown.

Results found for different parameters were compared and only one of the four parameters tested had a significant effect, the diffusion coefficient. Even adjustment of this parameter did not produce a good agreement with the experimental results. For a very high diffusion coefficient, particles did not follow the fluid flow and were mostly left at the surface. Decreasing of the diffusion coefficient produced results closer to the experimental ones, but when that parameter was decreased too much, diffusion became so weak that particles in the flow channels did not come close enough to the solid walls, and the second term in the exponential decay was too low. This behaviour was probably caused by the thin simulation geometry. Fitting parameters are shown only for the simulations where diffusion coefficient was changed only.

In almost all the simulations, a small hump can be seen in the ink distribution curve, which is not visible in the experimental result. It is known that confocal

Table 1: Comparison of fitting parameters for experimental and simulated results for varying diffusion coefficient.

Diffusion parameter	A1	A2	t1	t2	A1/A2
experiment	92.33075	48.53924	1.65710	12.37939	1.90219
0.008	81.63084	4.72173	1.90124	11.45980	17.28883
0.002	54.28106	9.90614	1.84410	11.43124	5.47954
0.0005	9.23625	2.45031	2.10995	12.24985	3.76942
0.0003	5.84310	1.55242	2.39962	13.33133	3.76387
0.0001	2.45893	0.62803	3.52730	13.65364	3.91531

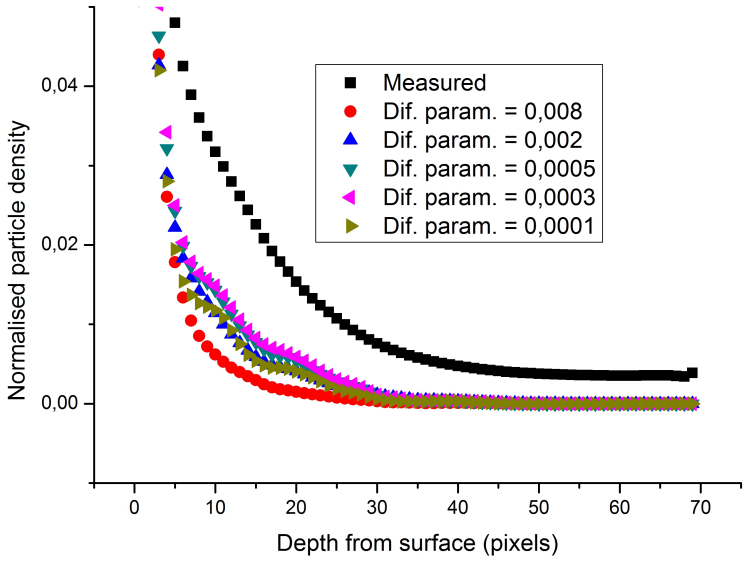

Figure 12: Results of simulations for varying diffusion coefficient together with the experimental result.

microscopy gives a weaker signal for increasing distances from paper surface. This of course generates discrepancy between simulations and experiments. The actual form of resolution decrease is not known, but using a linear correction the hump is also visible in the experimental result as shown in Fig. 16. In this case the correction makes the simulated and experimental results further apart however because this correction decreases the relative stregth of attachment in the surface layer. This is not relevant however, because the results should be different due to the thin surface layer in the simulation.

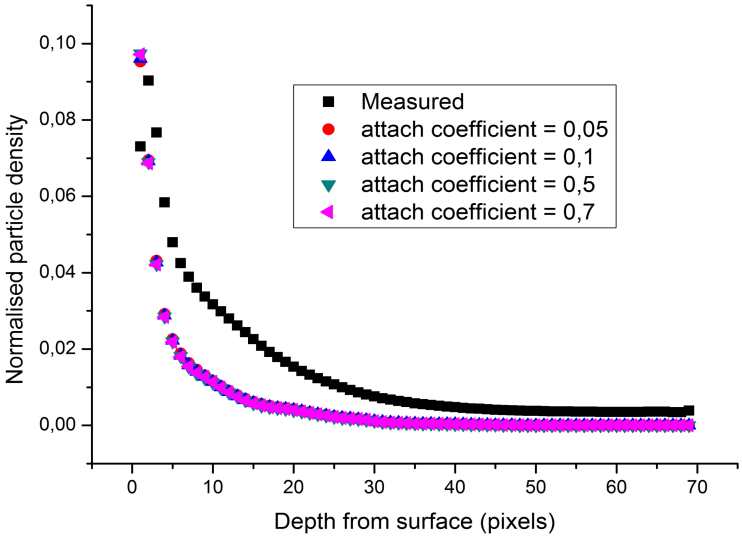

Figure 13: Results of simulations for varying attachment coefficient together with the experimental result.

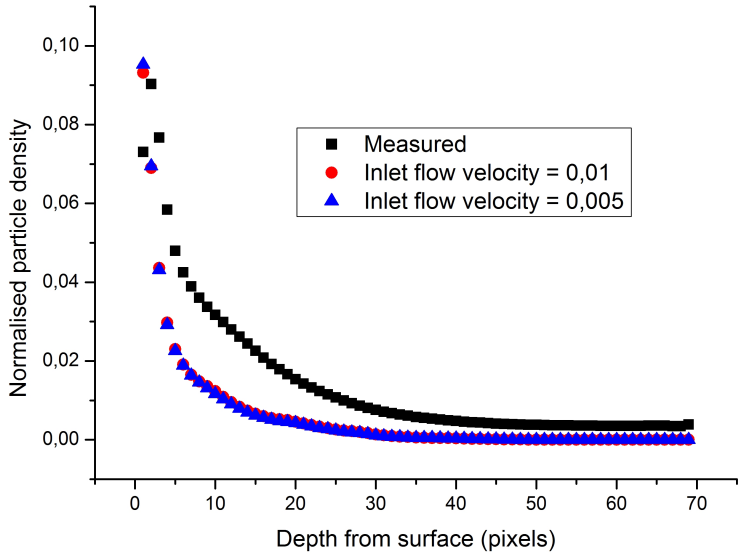

Figure 14: Results of simulations for varying inlet flow velocity together with the experimental result.

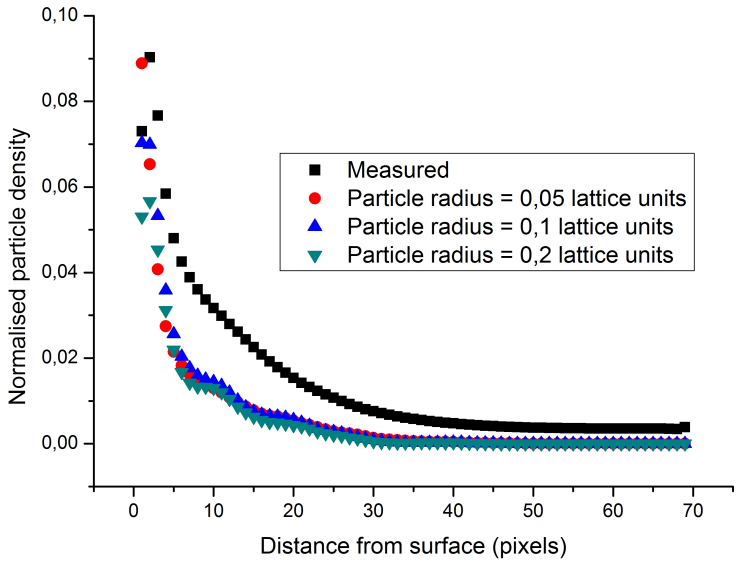

Figure 15: Results of simulations for varying particle radius together with the experimental result.

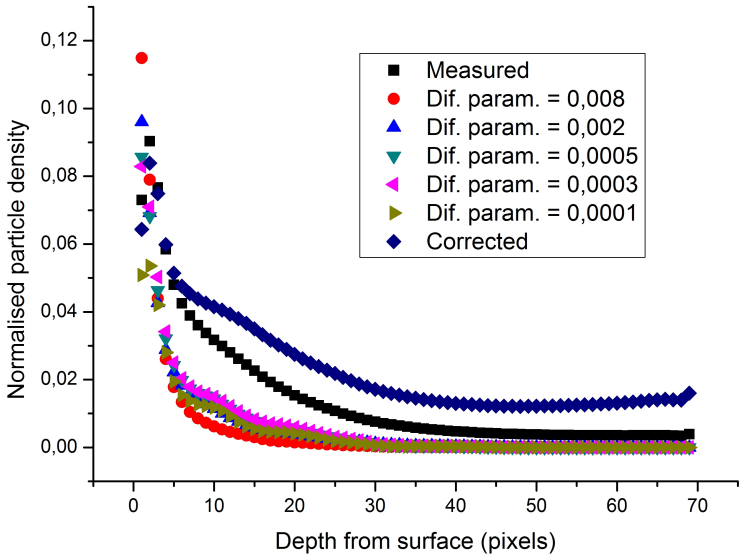

Figure 16: Results of simulations for varying diffusion coefficient together with the experimental result with and without linear correction.

5.2 Simulations in X-ray tomography images

As mentioned in the previous section, restrictions in the confocal microscopy imaging causes some discrepancy between simulated and experimental results caused by weakening of the signal as a function of distance from paper surface. With X-ray tomography this is not a problem. The whole sample can be imaged, and from that image a discretised simulation geometry can be formed. Unfortunately with this method the ink cannot be detected and compared with simulated results.

Two different simulation series were done in tomographic images. In the first series, a similar analysis as before was done: results for varying diffusion coefficient in the same (DL0591) sample were compared. It is evident from Fig. 17 and Table 2 that, by adjusting the diffusion coefficient, we can alter the $A1/A2$ ratio from surface dominance to convection dominance. This could not be achieved in simulation geometries produced by confogal microscopy. The reason for this lies probably in the fact that an X-ray tomographic image shows the whole thickness of paper and the simulation was done in a more realistic geometry.

Table 2: Comparison of fitting parameters of simulation results for varying diffusion coefficient in the DL0591 sample

Diffusion coefficient	A1	A2	t1	t2	A1/A2
0.004	31.0687	11.598	2.60143	15.156	2.678798
0.002	24.7018	18.2638	2.39178	27.6563	1.352501
0.0005	6.30858	11.4909	1.51977	133.035	0.549007

In the second simulation series, four different samples were studied with identical simulation parameters. The results of these simulations are shown in Fig. 18 and Table 3. The samples differed in the number of substances added to the paper. The first sample, DL0591, contained only the basic paper with no additives. Other samples were surface sized with water, starch and starch + salt in the order DL0946,DL0947 and DL0948.

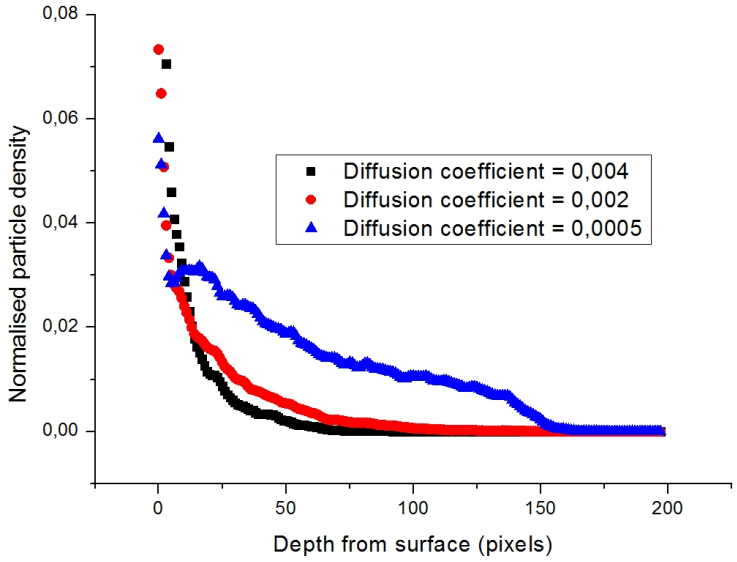

Figure 17: Results of simulations with different diffusion coefficient

Table 3: Comparison of fitting parameters with different samples. The A1/A2 ratios are compared between simulations and experimental results.

Sample	A1	A2	t1	t2	A1/A2 sim	A1/A2 exp
DL0591	31.0687	11.598	2.60143	15.156	2.678798	1.85922
DL0946	46.2487	10.8572	2.489	11.7293	4.259726	2.60306
DL0947	32.8266	4.48593	4.42992	21,2568	7,31768	3.78114
DL0948	29.4908	3.54001	3,6815	41.4423	8.330711	5.25461

Simulation results were also compared with experimental results based on confocal microscopy of these samples. As expected, the results are not identical because of many reasons. First of all, the simulation parameters were not chosen to produce the experimental flow situation. This kind of match for such a complex situation with a large number of parameters is hard or even impossible to find. Secondly, the experimental results were determined from confocal microscopy images which are not very relialable as mentioned above. What can be said however is that simulations and experiments both show the same tendency between the ratio $A1/A2$ and the amount of surface sizing used in the samples. The higher amount of surface sizing, the higher is the ratio $A1/A2$, i.e. a relat-

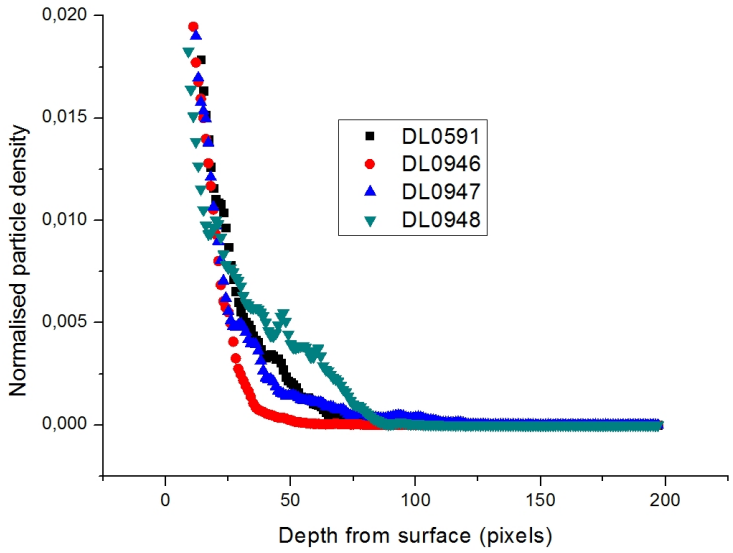

Figure 18: Results of simulations with different samples.

ively higher amount of ink has been attached in the surface.

The effect of sizing on the $A1/A2$ ratio was also studied by using another sample series in which the amount of surface and bulk sizing was altered. The four different cases were: (1) no surface or bulk sizing, (2) only surface sizing, (3) only bulk sizing and (4) surface and bulk sizing. The results were studied in the same way as for previous samples. Table 4 shows the fitting parameters for simulated and experimental results.

Table 4: Comparison of fitting parameters for different samples. The A1/A2 ratios are also given for simulated and experimental results. The numbers in the sample column relate to sample information as given above.

Sample	A1	A2	t1	t2	A1/A2 sim	A1/A2 exp
(1)1.0	63.31510	4.73711	1.08862	37.79190	13.36577	2.352951
(2)1.2	31.87110	3.45941	0.48619	59.46070	9.21287	5.274623
(3)5.0	28.36520	4.17250	0.50088	32.69140	6.79813	2.03805
(4)5.2	27.48740	2.72289	0.60255	41.65180	10.09494	5.325669

Because of discrepancies between the measured and simulated results, a more extensive simulation series was performed in order to find out if heterogeneity

of paper was partly responsible for the observed differencies. Four different simulations from different parts of the paper were performed for each sample, and the ink particle densities were determined as averages over the individual results. Figure 19 illustrates the choice of simulation geometries for the one and multiple simulation series. The results of the latter simulations are shown in Table 5

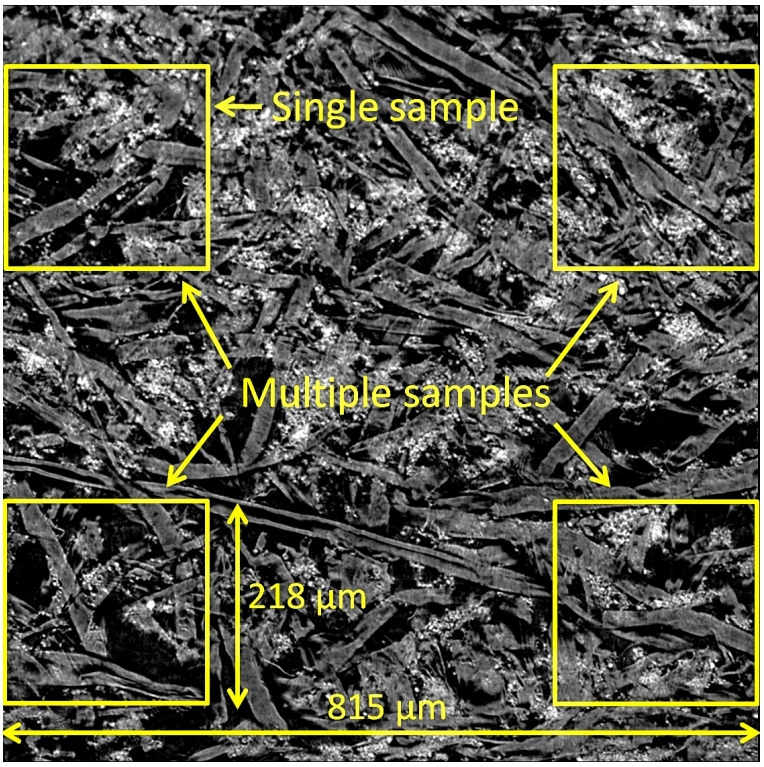

Figure 19: A cross section of a paper sample showing the choice of simulation geometries for the single and multiple simulation series.

Averaged results from many simulations did not agree any better with the experimental results, but the spread of the $A1/A2$ ratios decreased. Due to time constraints of the project, more extensive simulation series were not performed. Simulation series of an even larger amount of simulations per sample could have been used to see the values towards which the $A1/A2$ ratios eventually saturate.

Table 5: Comparison of fitting parameters determined as average values of four different simulations for each sample. The $A1/A2$ ratios are shown for averaged results and for results of a single simulation in each sample. The numbers in the sample column relate to sample information as given above.

Sample	A1	A2	t1	t2	A1/A2 Ave	A1/A2
(1)1.0	35.96200	4.04949	0.77923	50.29560	8.88062	13.36577
(2)1.2	28.62170	3.66994	0.49827	61.03550	7.79896	9.21287
(3)5.0	27.75170	3.19246	0.54670	63.80970	8.69289	6.79813
(4)5.2	27.24870	2.56581	0.59626	75.63520	10.61992	10.09494

6 Conclusions

In this study numerous simulations were performed to study ink particle propagation in several paper samples. Simulation results based on confocal microscopy images as the simulation geometry show qualitative similarity to experimental results, and they suggest that ink distribution in the sample is mainly controlled by the diffusion parameter of particle motion. This again tells us that the flow field strongly controls where the particles will go, unless their diffusion is strong enough to separate them from the main flow channels. Quantitatively the results differed however because of differencies in the actual paper structure and the geometry used in the simulations. Firstly, the image gained by the confocal microscopy technique shows only a small fraction of the thickness of the paper sample. Secondly, binarisation of the confocal microscopy image loses some information. The fine matter present in the real sample disappears in binarisation, which probably has a strong effect on ink particle propagation. The binarised geometry is however a fundamental part of the lattice-Boltzmann method, and the fine matter can only be modeled by introducing different kinds of discrete meshes between paper fibres. The threshold value of the binarisation could also be adjusted so that a larger part of fine matter is contained in the binary image, but then also disturbances in the image can be interpreted as solid.

To be able to produce similar behaviour as seen in the experimental results, another imaging technique was used. In X-ray tomography the whole thick-

ness of the paper sample could be included, and thus one source of discrepancy between simulations and experiments could be eliminated. Unfortunately the ink could not be seen with this technique, and comparison between simulations and experiments could not be made. It was observed however that with the full thickness of paper included the simulation parameters, mainly diffusion of the particles, could be adjusted so as to produce strong attachment to surface or alternatively to deeper down in the paper sample. For better comparison between the simulations and experiments, a more sophisticated image acquiring technique should be constructed. One possibility is to carefully mark the location where the image should be taken and then acquire the image by using both confocal microscopy and X-ray tomography. This way the whole thickness and also the attached ink could be observed. Another possibility would be to use ink that shows up in the X-ray tomography image. Such an ink is certainly possible to manufacture, but was not available in the present study.

X-ray tomography images were also used to simulate paper samples for varying surface and bulk sizing. For these samples experimental results based on confocal microscopy were also available. The first simulation series of varying surface sizing gave promising results. Both simulations and experiments showed a similar tendency, a high amount of surface sizing increased the amount of particles left near the surface. The second simulation series where different amounts of surface and bulk sizing were used, did not give as good results. A statistical simulation series where multiple simulations were done for each sample was conducted to decrease the effect of paper heterogeneity on the results. The results did not change considerably, which can occur due to many reasons. Firstly, the amount of simulations can still be too small. The physical area of the sample in each simulation was only $(200\ \mu m)^2$. In this length scale the heterogeneity of paper is very visible as the individual paper fibres are about 10 μm wide. More statistics may thus be needed for reliable results. Secondly, even though there would be enough statistics in a certain area of paper, and the results would be relialible, we would not know that these results represent the paper as a whole. Simulations in entirely different parts of the paper are thus necessary. Thirdly, the chemical phenomenon related to particle attachment

is modelled with one attachment coefficient throughout the entire paper thickness. This may not be the right approach, surface sizing for example effectively changes surface attachment without affecting the deeper parts of the paper. In the confocal microscopy simulations it was observed that the attachment coefficient did not play a vital part in the results, so this is probably not the first issue that should be considered.

In summary, the lattice-Boltzmann method shows great potential for analysis of ink settling in paper, but much more work has to be done before it can be reliably used to predict the print quality. Future work involves development of image acquiring techniques and ways to deal with the inherent heterogeneity of the paper.

References

[1] Harris S, *An introduction to the theory of the Boltzmann equation*, republication, Dover Publications, New York, 2004

[2] Succi S, *The lattice Boltzmann equation for fluid dynamics and beyond*, Oxford University Press, Oxford, 2001

[3] White F, *Fluid Mechanics, sixth edition*, McGraw-Hill, New York, 2008.

[4] Adams R, *Calculus: a complete course, sixth edition*, Pearson, Toronto, 2006

[5] Flanders H, *Differentiation Under the Integral Sign*, The Ame. Math. Mont. **80**(6):615, 1973

[6] Garcia-Colin L, Velasco R, and Uribe F, *Beyond the Navier-Stokes equations: Burnett hydrodynamics*, Phys. Rep. **465**(4):149, 2008

[7] Reese J, Gallis M and Lockerby D, *New directions in fluid dynamics: non-equilibrium aerodynamic and microsystem flows*, Phil. Trans. R. Soc. Lond. Ser.A Math. Phys. Eng. Sci. **361** (1813): 2967, 2003

[8] Bowley R, Sánches M, *Introductory Statistical Mechanics, second edition*, Oxford University Press, New York, 1999

[9] Thornton S and Marion J, *Classical Dynamics of Particles and Systems*, fifth edition, Brooks/Cole, 2004

[10] Alekseev B, *Generalized Boltzmann Physical Kinetics*, Elsevier, Amsterdam, 2004

[11] Gilberto M, *An Introduction to the Boltzmann Equation and Transport Processes in Gases*, Springer, Heidelberg, 2010

[12] Boltzmann L, *Weitere Studien über das Wärme gleichgenicht unfer Gasmoläkuler*, Sitzungsberichte Akad. Wiss. **66**: 275, 1872.

[13] Villani C, *A Review of Mathematical Topics in Collisional Kinetic Theory*, Handbook of Mathematical Fluid Dynamics **1**: 71, Elsevier Science, Amsterdam 2002.

[14] Shan X, *Kinetic theory representation of hydrodynamics: a way beyond the Navier-Stokes equation*, J. Fluid Mech. **550**: 413, 2006

[15] Chavanis P-H, *Generalized thermodynamics and kinetic equations: Boltzmann, Landau, Kramers and Smuluchowski*, Elsevier, Physica **332** A: 89, 2004

[16] Bellomo N, *From the Boltzmann Equation to Generalized Kinetic Models in Applied Sciences*, Elsevier, Mathl. Comput. Modelling **26** (7): 43, 1997

[17] Ferziger J and Perić M, *Computational Methods for Fluid Dynamics*, Springer, Heidelberg, 1997

[18] Qian Y, d'Humières D and Lallemand P, *Lattice BGK Models for Navier-Stokes Equation*, Europhys. Lett. **17** (6): 479, 1992

[19] Maxwell J, *On the dynamical Theory of Gases*, Phil. Trans. R. Soc. Lond. **157**: 49, 1867.

[20] Mattila K, *Implementation Techniques for the Lattice Boltzmann Method*, Jyväskylä Studies in Computing 117, 2010

[21] Raabe D, *Overview of the lattice Boltzmann method for nano- and micro-scale fluid dynamics in materials science and engineering*, Modelling Simul. Mater. Sci. Eng. **12**: R13, 2004

[22] Chikatamarla S and Karlin I, *Lattices for the lattice Boltzmann method*, Phys. rev. E **79**: 046701, 2009

[23] Ginzburg I, Verhaeghe F and d'Humières D, *Two-Relaxation-Time Lattice Boltzmann Scheme: About Parametrization, Velocity, Pressure and Mixed Boundary Conditions*, Commun. Comput. Phys. **3** (2): 427, 2008.

[24] Ginzburg I and d'Humières D, *Multireflection boundary conditions for lattice Boltzmann models*, Phys. Rev. E **68**(6): 066614, 2003

[25] Premnath K and Abraham J, *Three-dimensional multi-relaxation time (MRT) lattice-Boltzmann models for multiphase flow*, Jour. of Comput. Phys. **225**(2): 539, 2007

[26] Rui D, Baochang S and Xingwang C, *Multi-relaxation-time lattice Boltzmann model for incompressible flow*, Elsevier, Phys. Let. A **359**(6): 564, 2006

[27] Chen F, Xu A, Zhang G and Li Y, *Multiple-relaxation-time lattice Boltzmann model for compressible fluids*, Elsevier, Phys. Let. A **375** (21): 2129, 2011

[28] Fan L-S and Zhu C, *Principles of gas-solid flows*, Cambridge University Press, New York, 1998